International Journal of Solids and Structures 264 (2023) 112098

Contents lists available at ScienceDirect

International Journal of Solids and Structures

journal homepage: www.elsevier.com/locate/ijsolstr

Statistical effects of pore features on mechanical properties and fracture behaviors of heterogeneous random porous materials by phase-field modeling

Yutai Su [a], Jiaqi Zhu [a], Xu Long [a,*], Liguo Zhao [b], Chuantong Chen [c], Changqing Liu [b,*]

[a] School of Mechanics, Civil Engineering and Architecture, Northwestern Polytechnical University, Xi'an 710129, China
[b] Wolfson School of Mechanical, Electrical and Manufacturing Engineering, Loughborough University, Leicestershire LE11 3TU, United Kingdom
[c] The Institute of Scientific and Industrial Research, Osaka University, Mihogaoka 8-1, Ibaraki, Osaka 567-0047, Japan

ARTICLE INFO

Keywords:
Pore feature distributions
Random porous materials
Fracture phase-field model
One-cut Gaussian random field
Sintered silver nanoparticles

ABSTRACT

Heterogeneous materials with randomly distributed pores are ubiquitous, such as sintered silver nanoparticles, concrete materials, 3D printed polymers, and natural bones. Recent experimental investigations have revealed that porosity and also pore-related geometries (size, number, shape, distribution and alignment) have significant impacts on the mechanical behavior of random porous materials. However, existing studies focus on the porosity effect while ignoring other pore features such as pore size and pore shape. Our research is dedicated to a computational framework for generating isotropic/anisotropic random porous materials using Gaussian random fields with stochastic pore size and shape factor and addressing the mechanical properties and behavior of brittle fractures using a fracture phase-field model with a preferred degradation function. Sintered silver nanoparticles with typical randomly distributed pores, as representative porous materials, are chosen for their promising applications in emerging fields such as power electronics and wearable devices. In order to emphasize the effect of pore size and shape, 420 random samples with a fixed porosity were generated to discuss the stress–strain response during fracture and to establish statistical relationships between pore feature distributions and mechanical properties such as Young's modulus, UTS, and average historical energy. Our findings suggest that the statical attributes of the pore sizes and shape factors significantly affect the material performance related to the mechanical properties and fracture behavior, which could give a better understanding of the random porous materials and guide reliability-based material design optimization.

1. Introduction

Nowadays, sintered silver nanoparticles, a promising candidate for electronics interconnection materials, are widely adopted in emerging electronics technologies such as next-generation power electronics (Ding et al., 2021), polymeric devices (Chiappone et al., 2018), skin-mounted devices (Sanchez-Romaguera et al., 2015), printable elastic conductors (Matsuhisa et al., 2017), and wearable printed circuits (Zhang et al., 2020). Owing to its low sintering temperature, high melting point, and excellent thermal and electrical conductivities, sintered silver nanoparticles allow reliable electrical and mechanical interconnects to be used for various substrates and harsh environments. Generally, silver nanoparticle ink or paste is prepared with silver nanoparticle powder dispersed in organic components. During the sintering process, organics among silver nanoparticles are removed by means of thermal sintering (Chen and Suganuma, 2019), laser sintering (Liu et al., 2021), infrared sintering (Chen et al., 2020), microwave sintering (Jung et al., 2016), and chemical sintering (Okada et al., 2019). Exposed nanoparticles with a high surface free energy can be rapidly linked together by interconnecting and necking to form coarse-grained and densified porous structures. However, A massive number of pores in the sintered structure cannot be entirely removed due to low temperature and low-pressure conditions, even at room temperature and pressureless environments. The pores induce considerable uncertainties in the material properties of sintered silver nanoparticles, such as Young's modulus, shear strength, and fracture toughness.

Several studies have attempted to establish the relationships between porous microstructures and the mechanical properties of sintered

* Corresponding authors.
E-mail addresses: xulong@nwpu.edu.cn (X. Long), C.Liu@lboro.ac.uk (C. Liu).

https://doi.org/10.1016/j.ijsolstr.2022.112098
Received 16 June 2022; Received in revised form 20 December 2022; Accepted 27 December 2022
Available online 29 December 2022
0020-7683/© 2022 The Author(s). Published by Elsevier Ltd. This is an open access article under the CC BY license (http://creativecommons.org/licenses/by/4.0/).

silver nanoparticles (Chen and Suganuma, 2019; Cham, 2019; Zabihzadeh et al., 2017). Porosity has been widely investigated in previous works as one of the critical factors impacting the mechanical properties and fracture behavior of random porous structures (Marvi-Mashhadi et al., 2021; Vazic et al., 2021). Numerous experiments reveal that porosity in sintered silver nanoparticles has a significant effect on Young's modulus, yield strength, ultimate tensile strength (UTS), strain to failure, and fracture toughness. It is extremely challenging to obtain the statistical results through in-situ testing of a large number of *meso*-scale random porous structures, our previous work investigated the effects of porosity on Young's modulus, UTS, and strain to failure using the phase-field model approach and obtained numerical results that are consistent and in good agreement with experimental results (Su et al., 2021). However, the pore network's characteristics include not only porosity but also their size, number, shape, and distribution, which are essential to the mechanical properties of random porous materials (Watring et al., 2022). Choe *et al.* (Choe et al., 2018) performed thermal aging on the sintered silver, which resulted in changes in microscopic characteristics such as pore size and grain size. The tensile strength and fracture mode of micro-porous silver are affected by pore size, grain size, and porosity in a complicated and significant way. Meanwhile, the influence of pore shapes in the sintered silver materials cannot be ignored, so the statistical distributions of shape factors during pore formation and thermal aging are investigated. Zubir *et al.* (Mohd Zubir et al., 2019) attempted several processing settings in order to sinter silver nanoparticles. The distributions of both pore size and form factor in cross-section morphologies were statistically investigated, and it was found that the sintering temperature, pressure, and duration, as well as heating rate, have significant effects. Besides, Tan *et al.* (Tan et al., 2020) conducted thermal aging tests at temperatures ranging from 125 °C to 350 °C, and counted the corresponding distributions of pore size and shape factor. Non-in situ shear testing revealed strong correlations between shear strength and the distributions of pore size and shape factor. Moreover, the pore feature distributions of random porous materials have considerable differences, especially for pressureless and low-pressure sintering (Lee and Lee, 2021). As a result, when simulating and analyzing a random porous structure, the distribution of pore features in the pore network should be taken into account. The pore characteristics of sintered silver nanoparticles are always statistically assessed after destructive tests, hence microscopic statistical in situ tests are extremely complicated and costly. Therefore, an approach to describe random porous materials and simulate the fracture process is greatly anticipated to give the statical relationships between pore feature distributions and mechanical behavior for a characterized random porous structure.

Statical descriptors for random heterogeneous materials are primary and fundamental to reconstructing the sintered silver nanoparticles. Gaussian random fields, describing the points in some space as a multivariate Gaussian distribution, are widely used in the modeling of random porous media (Jiang et al., 2013), geostatistical spatial fields (Fuglstad et al., 2019), and medical and biological images (Burt et al., 2020). Neumann *et al.* (Neumann et al., 2019) constructed a three-phase microstructure model using a Gaussian random field containing silver-, polytetrafluorethylene-, and pore-phases. The porous structure of the material sample was obtained by focused ion beam (FIB), which was compared with the model realization finding similarities in the spatial continuous phase size distribution. Additionally, a large number of structures can be generated to predict material properties statistically (Stenzel et al., 2017). Blatny *et al.* (Blatny et al., 2021) investigated the micromechanics of porous brittle solids, proposing a single-cut Gaussian random field microstructure to institute the porous media's spherical/particulate model. Based on the Gaussian random field model, the finite size effects, discretization errors, and statistical structural fluctuations were discussed for a typical porous media. However, the above research focused on uniformly isotropic microstructures, whereas random porous materials with structural anisotropy should be explored further. Gao *et al.* (Gao et al., 2021) developed microstructure models of a variety of random heterogeneous materials, ranging from two to three dimensions, two to multi-phase, and isotropic to anisotropic. They discovered that the distribution attributes of material properties differ between isotropic and anisotropic microstructures. Further, Zerhouni *et al.* (Zerhouni et al., 2021) investigated the effect of parameters such as porosity and pore aspect ratio on elastic parameters such as bulk modulus and shear modulus in an isotropic random porous structure. These studies investigated mechanical properties but only focused on elastic properties without taking fracture processes into account. Meanwhile, the pore feature parameters are only discussed as a single value or mean value, failing to establish the correlation between the pore feature distribution and mechanical properties. This motivates this study to establish isotropic or anisotropic Gaussian random fields for describing the random porous structure of heterogeneous materials, as well as to investigate the correlation between pore feature distributions and material properties in depth.

Moreover, fracture phase-field models were employed to describe the stress–strain responses and fracture behavior of materials driven by various types of energies, such as elasto-plastic (Duda et al., 2018; Fang et al., 2019), thermo-elastic (Miehe et al., 2015); viscoelastic (Yin and Kaliske, 2020), elasto-viscoplastic (Cheng et al., 2017); and chemo-mechanical energies (Miehe et al., 2016; Schuler et al., 2020). Also, the highly accurate degradation functions of the fracture phase-field model were thoroughly investigated (Arriaga and Waisman, 2018; Kuhn et al., 2015; Sargado et al., 2018). Based on the fundamentals of phase-field models, Eid *et al.* (Eid et al., 2021) detailed the effective elastic, toughness, and strength properties of three microstructures at the mesoscopic scale in a multiscale analysis of brittle fracture in heterogeneous porous materials. Chen *et al.* (Chen et al., 2019) investigated crack deflection and penetration in a heterogeneous microstructure and accurately predicted the effect of grain boundary sizes on the crack path. Cao *et al.* (Cao et al., 2020) proposed an FFT-based phase-field model to solve stress–strain and crack phase field problems of heterogeneous materials with high efficiency. In addition, Ernesti *et al.* (Ernesti et al., 2020) addressed phase-field crack issues for heterogeneous microstructures and acquired the crack surface and stress–strain response of the fiber-reinforced composites. The fracture phase-field model is a powerful tool to predict the mechanical properties and fracture processes in heterogeneous microstructures (He et al., 2022; He et al., 2020).

In this study, we proposed a one-cut Gaussian random field model to describe isotropic or anisotropic random porous structures for sintered silver nanoparticles under pressure and pressureless conditions. A statistical analysis of pore size and shape factor was conducted to understand the feature lengths in the Gaussian random field model. Furthermore, a fracture phase-field model with a proper degradation function was adopted to match the brittle fracture of sintered silver materials. Based on the above models, the stress–strain responses of the 420 generated samples with varying pore features, such as pore sizes and shape factors, were computed throughout the fracture process. The mechanical properties of the 420 samples were also calculated and analyzed, including Young's modulus, UTS, and average historical energy at the maximum stress point. In addition, an exploratory analysis of the sample sets was carried out to investigate the relationships between pore feature distributions and the mechanical behavior of sintered silver nanoparticles. The proposed framework and numerical models were also applicable to other heterogeneous random porous materials.

2. Computational framework

2.1. General statements

This study aims to develop a better understanding of the relationship between microstructure attributes and macroscopic mechanical properties of the sintered silver nanoparticles. First, the sintered silver nanoparticles are typical two-phase random heterogeneous materials with pore and solid phases. A mathematical model of the spatial statistical features is proposed using a Gaussian random field approach with a

constant cutting plane to describe the random heterogeneous material. Based on the cutting Gaussian random samples, massive voxel-based material matrices are generated to represent the random porous structures with specific microstructure attributes. To thoroughly discuss the sintered silver nanoparticles under varying temperatures and pressures, both isotropic and direction-related pore shapes, especially flattened pore shapes, are considered in the model. Due to the accessible and adjustable sample size, further statistical analysis can be performed on the sintered silver nanoparticles. Secondly, the fracture phase-field approach is adopted to simulate the mechanical behavior during the fracture process and of generated samples. Multiple cracks grow parallelly in random porous structures with isotropic mechanical and fracture properties. On account of brittle fracture features in the sintered silver nanoparticles, a highly accurate degradation model is chosen to describe the stiffness matrix degradation during fracture. In addition, we assume the effect of the porous structure is greater than that of grain boundaries. Therefore, grain boundaries are not considered in this model. Combining Gaussian random field and phase-field approaches, microscopic stochastic porous morphologies, and macroscopic mechanical properties are analyzed with a sizable random sample.

In this section, we use a two-dimensional tensile specimen with random pores to simulate the mechanical properties and fracture behavior. Based on previous numerical studies (Su et al., 2021; Su et al., 2021), the specimen size is 20 μm × 20 μm, and the quadrilateral element is 0.2 μm × 0.2 μm, satisfying the convergence and computational requirements. Thus, the sample is meshed to 100 × 100 equal-sized voxels, as shown in Fig. 1. For microstructure attributes of Gaussian random fields, the feature length of the random pore ranges from 1.0 to 10.0 times element length, that is, from 1/100 to 1/10 of specimen length. Twenty samples are randomly constructed for each set of feature lengths, up to 420 samples. The boundary conditions of pure tensile loading are illustrated in Fig. 1. An upward displacement is applied to the top edge of the model. The reaction force at the top edge is calculated as an essential and notable output to acquire the stress–strain response. Accordingly, essential mechanical properties of the generated samples, such as Young's modulus and UTS, could be derived from the numerical predictions. Considering the gradual degradation of the solid phase materials and the continuous description of the smeared crack, a phase-field model with an exponential degradation function is employed to simulate the complete fracture process of random porous structures. Following the previous work (Su et al., 2021; Molnár et al., 2020), a two-layered finite element framework is implemented in Abaqus and its subroutines. Especially, the UEL (user defined element) subroutine is developed to calculate the phase-field values in the first layer. Via common variables in the subroutines, the degradation scaling values are delivered to the stiffness matrix of the solids in the second layer. Then, history elastic energies during degrading are returned to the first layer to drive the increase in the phase-field value. This staggered computational scheme is adopted and detailed in Section 2.3. Furthermore, because the maximum stress point is critical for material properties and fracture behavior, we chose the average history energy at this point as a remarkable output to investigate the energy absorption and material degradation of the random porous materials prior to severe condensation.

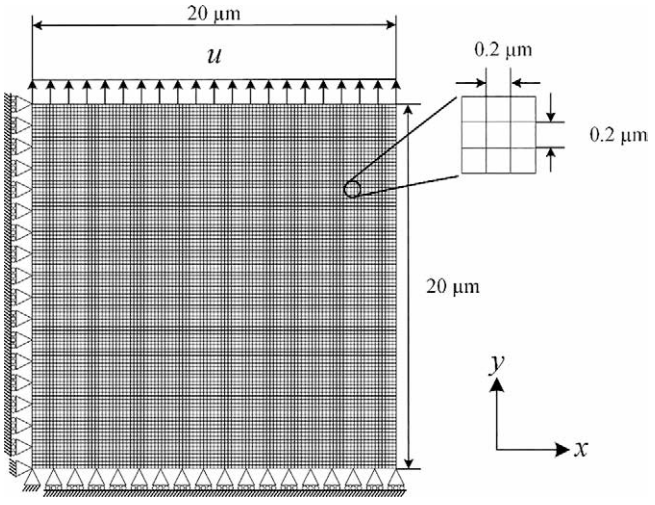

Fig. 1. Geometries and boundary conditions for the voxel-based specimen.

2.2. Microstructural model of random porous structures

To describe and present the spatial stochastic properties of the sintered silver nanoparticles, the Gaussian random field model is chosen on account of its effectiveness and robustness in random sample generation (Gao et al., 2021; Liu et al., 2019; Zein et al., 2019). Gaussian random field model could produce a certain number of two- or three-dimensional normalized spatial probability distributions. Then, a fixed threshold value can be assigned not only to transform the spatial probability distribution into binary distribution (with zero representing the solid and one representing the pore) but also to determine the target porosity of the structures. The Gaussian random field model with adjustable threshold values is developed to generate the random porous microstructures.

Assume that X is a real-valued stationary Gaussian random field on $\mathbb{R}^d$, where d is the dimensional number of the spatial model. For any collection $\boldsymbol{s} = \{\boldsymbol{s_1}, \boldsymbol{s_2}, \ldots, \boldsymbol{s_n}\}$ of finite locations, the joint distributions of $X = \{X(\boldsymbol{s_1}), X(\boldsymbol{s_2}), \ldots, X(\boldsymbol{s_n})\}$ is multivariate Gaussian. The mean function of the Gaussian random field model is $\mu(\boldsymbol{s}) = E[X(\boldsymbol{s})]$, and the covariance function is $\gamma(\boldsymbol{s}, \boldsymbol{s'}) = C(\boldsymbol{h}) = Cov\{X(\boldsymbol{s}), X(\boldsymbol{s'})\} = E[(X(\boldsymbol{s}) - \mu(\boldsymbol{s}))(X(\boldsymbol{s'}) - \mu(\boldsymbol{s'}))]$, where $\boldsymbol{h} = \boldsymbol{s} - \boldsymbol{s'}$. The probability density function of the Gaussian random field model in the locations $\boldsymbol{s} = \{\boldsymbol{s_1}, \boldsymbol{s_2}, \ldots, \boldsymbol{s_n}\}$ could be defined as

$$p(X(\boldsymbol{s_1}), X(\boldsymbol{s_2}), \cdots, X(\boldsymbol{s_n})) = \frac{1}{(2\pi)^{n/2}(\det \boldsymbol{C})^{1/2}} \times \exp\left\{ -\frac{1}{2}(\boldsymbol{s} - \boldsymbol{\mu}(\boldsymbol{s}))^T \boldsymbol{C}^{-1}(\boldsymbol{s} - \boldsymbol{\mu}(\boldsymbol{s})) \right\} \tag{1}$$

where

$$\boldsymbol{\mu}(\boldsymbol{s}) = \begin{bmatrix} E[X(\boldsymbol{s_1})] \\ \vdots \\ E[X(\boldsymbol{s_n})] \end{bmatrix} \tag{2}$$

and

$$\boldsymbol{C} = \begin{bmatrix} \gamma(\boldsymbol{s_1}, \boldsymbol{s_1}) & \cdots & \gamma(\boldsymbol{s_1}, \boldsymbol{s_n}) \\ \vdots & \ddots & \vdots \\ \gamma(\boldsymbol{s_n}, \boldsymbol{s_1}) & \cdots & \gamma(\boldsymbol{s_n}, \boldsymbol{s_n}) \end{bmatrix}. \tag{3}$$

Let the Gaussian random field be on a two-dimensional Euclidian space, and the mean value of the Gaussian random field be zero. Here, a Gaussian autocovariance function $\gamma(\boldsymbol{s_i}, \boldsymbol{s_j})$ could be defined as

$$\gamma(\boldsymbol{s_i}, \boldsymbol{s_j}) = C(\boldsymbol{h_{ij}}) = C(|\boldsymbol{s_i} - \boldsymbol{s_j}|) = e^{-\frac{(x_i - x_j)^2}{\lambda_x^2} - \frac{(y_i - y_j)^2}{\lambda_y^2}} \tag{4}$$

where λ_x and λ_y, are the correlation lengths in the x- and y- directions, representing the characteristic lengths of the two-dimensional spatial distribution in the x- and y-direction, respectively. Isotropic random fields could be generated when λ_x is equal to λ_y, and anisotropic random fields can be constructed by setting different values of λ_x and λ_y.

Based on the above Gaussian random field model, spatial probability distributions with the size of 100 × 100 are generated and shown in Fig. 2. Different combinations of correlation lengths in the x-direction and y-direction are selected. Fig. 2 (*a*) to (*c*) show three realizations of the Gaussian random field with the same λ_x and λ_y, taking the values of 3.0, 5.0, and 10.0, respectively. For all three distributions, the shape directions of the multivariate Gaussian distributions show an overall isotropy, both

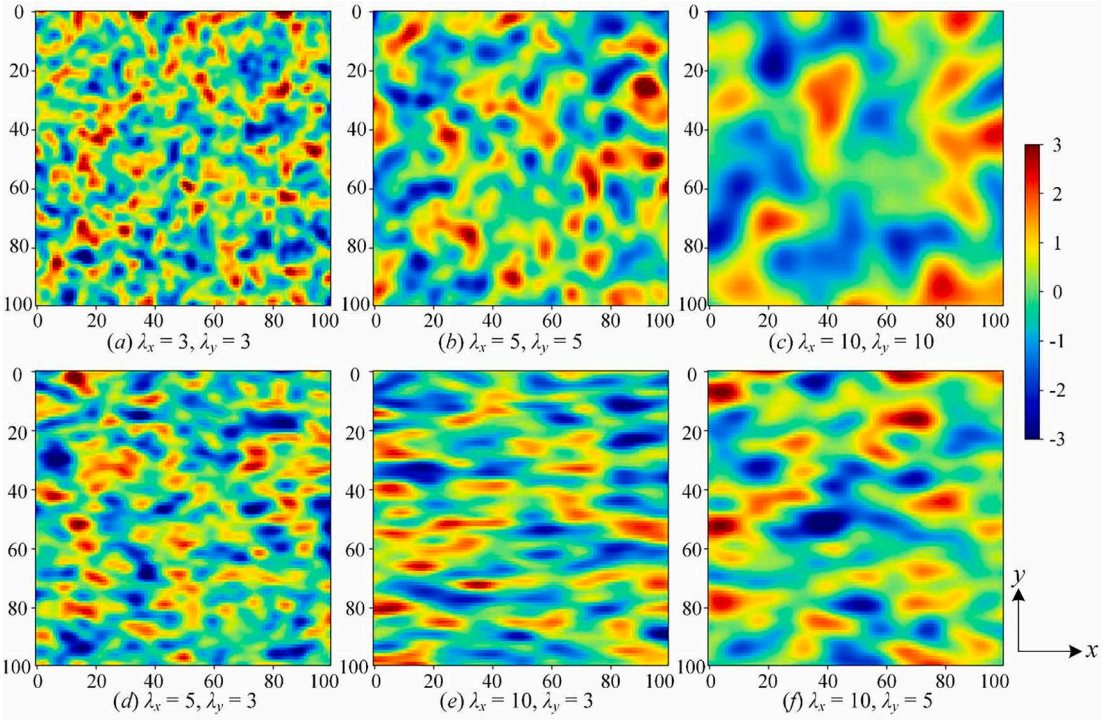

Fig. 2. 100 × 100 spatial Gaussian random field distributions with different combinations of λ_x and λ_y.

spatially and statistically. The average spans of the single-peak distributions are approximately the same in both *x*- and *y*-direction. Also, the span of the single-peak distribution increases with the increase of the correlation length. For simulating the flattened pore shapes under given pressure and temperature, given combinations with different λ_x and λ_y are determined where λ_x is larger than λ_y. Fig. 2 (*d*) to (*f*) present three anisotropic shape distributions of the Gaussian random field realizations. Similarly, with the isotropic shape distributions, the parameters λ_x and λ_y are positively related to the average spans of the single-peak distribution in the *x*- and *y*-direction, respectively. Here, the absolute values of λ_x and λ_y decide the size of the shape distribution, and the relative ratio of λ_x and λ_y determines the flattening degree of the shape distribution. Hence, the correlation lengths λ_x and λ_y are utilized to manipulate the shape distribution features, including anisotropy or isotropy, shape size, and aspect ratio.

Gaussian random field distributions are continuous numerical realizations in the sample space. However, the sampling target is a random porous structure with a discrete pore phase and solid phase distributed. To transform the Gaussian random field samples to the binary spatial samples, a cut-level indicator function I with constant thresholding is utilized, shown as

$$I(x, y, F_0) = \begin{cases} 1, & \text{if } Z(x, y) > F_0, \\ 0, & \text{if } Z(x, y) \le F_0, \end{cases} \tag{5}$$

where F_0 is the constant threshold value to classify the Gaussian random field sample into two-phase regions. When the sample value Z is above the cut-level plane of F_0, the located pixel area is defined as the pore phase. Otherwise, the pixel area is set as solid. Accordingly, a specific amount of two-phase random porous structures is sampled and realized. Since this study focuses on the pore shape and distribution, the porosity of the generated samples is fixed to avoid the possible effects of gross porosity. To achieve a given porosity, an optimization algorithm is proposed to determine the threshold value F_0, the position of the cut-level plane, shown in Box 1.

Box 1
The optimization algorithm to generate the random porous sample with a given porosity.

1. Generate the random sample $Z(x, y)$ by the Gaussian random field model in a sample space ($N_x \times N_y$) as shown in Fig. 1. Here, N_x is the point number in the *x*-direction, and N_y is the point number in the *y*-direction.
2. Initialize the value Z_0 for F_0. For the given porosity P, the initial value Z_0 for F_0 is calculated by the inverse function of cumulative Gaussian distribution as $\Phi^{-1}(1 - P)$.
3. Determine the target number n of the pore area as $N_x \times N_y \times P$.
4. Count the current number m of the pore area where the $Z(x, y)$ is greater than F_0.
5. Optimize the threshold value F_0 to achieve the minimum distance d_{mn} between m and n by repeating the fourth step. The optimization equation is defined as
   Minimize: $d_{mn} = |m - n|$
   Subject to: $n = N_x \times N_y \times P$
   $m = \sum_{x=1}^{N_x} \sum_{y=1}^{N_y} I(x, y, F_0)$
6. Obtain the optimized threshold value F_0 and target sample of the random porous structure.

Utilizing the proposed algorithm, the cut-level plane of F_0 is determined, and cut the Gaussian random field into a two-phase porous structure with a given porosity P of 20.0 %, shown in Fig. 3. As the random sample without regard to any spatial positions follows the standardized normal distribution, the cut-level plane of F_0 is located around the plane of the initial value $Z_0 = \Phi^{-1}$ (0.80), computed as 0.8462. For the six samples in Fig. 3, the values of F_0 are ranging from 0.7875 to 0.9492, which have a mean value of 0.8653. The initial value in this algorithm allows an efficient optimization to quickly reach the target porosity.

Next, the one-cut Gaussian random field samples are transformed into two-value binary random porous samples, shown in Fig. 4. Pore size, pore shape, and pore distribution in the one-cut Gaussian random field samples have a greater degree of spatial randomness and fewer certainties. The figure indicates that the pore shape and distribution of the random samples are correlated with the values of λ_x and λ_y. The correlation lengths λ_x and λ_y affect the average sizes of the pores in the x- and y-directions, respectively. Fig. 4 (*a*) to (*c*) are isotopically distributed with random pores, some of which are partially connected to others. Disregarding the connective pores, the minimum unit pore in the isotropic structure has a small aspect ratio and an area size positively related to the correlation lengths. Fig. 4 (*d*) to (*f*) are anisotropic random porous structures with flattened pores. The aspect ratio of the pores mainly depends on the ratio of λ_x and λ_y. Consequently, the flatness of the pores increases in the order of Fig. 4 (*d*), (*f*), and (*e*). Meanwhile, the average area of the minimum unit pore is directly associated with the product of λ_x and λ_y, rising in the sequence of Fig. 4 (*d*), (*e*), and (*f*).

To ensure the validity and stability of the pore distribution features statically, 120 random samples of random porous structures are generated for six equally sized groups, including Group 1 ($\lambda_x = 3$, $\lambda_y = 3$), Group 2 ($\lambda_x = 5$, $\lambda_y = 5$), Group 3 ($\lambda_x = 5$, $\lambda_y = 5$), Group 4 ($\lambda_x = 5$, $\lambda_y = 3$), Group 5 ($\lambda_x = 10$, $\lambda_y = 3$), and Group 6 ($\lambda_x = 10$, $\lambda_y = 5$). Statistical analyses of the pore number, distributions, and shape factors of the 120 random samples are carried out.

The closed pores, surrounded by impenetrable solids, in the random samples from the six groups are counted, shown in Fig. 5. Here, the order of the six groups follows that of the average pore numbers. The product of the two correlation lengths, λ_x and λ_y, is directly related to the pore numbers of the random porous structures. Because the porosity and total area of each sample are fixed at 0.20 and 20 × 20 μm^2, the area of all pores is a constant, equal to 80 μm^2. When the average area of the minimum unit pore is small, the pore number is inevitably large in porous structures with a fixed pore area. Meanwhile, the random samples present the stochastic features of the pore number, essentially following the normal distributions. The mean value of the pore number in each group distinctly differs from the correlation lengths, and the fluctuation ranges of the pore number decrease with the decreasing mean values.

Pore size (S_{pore}), or the area of each closed pore, is statistically counted for each of the samples within the six groups. Accordingly, the distributions of the pore size for Group 1 to Group 6 are obtained and shown in Fig. 6. Each sample is identified by a particular gradient color, and its contributions to the pore size distributions are detailed. Fig. 6 (*a*) to (*c*) show that the pore size distribution gradually shifts toward larger pore sizes as the correlation lengths increase. Meanwhile, Fig. 6 (*d*) to (*f*) indicate the pore size distributions for the anisotropic porous samples tend to move rightward, with the product of the correlation lengths λ_x and λ_y increasing. Overall, the mean of the pore sizes for each group is positively correlated with the product of the correlation lengths, and the order of the groups by the mean of the pore sizes is the reverse of the order by the pore number, that is Group 3, Group 6, Group 5, Group 2, Group 4, and Group 1 from largest to smallest. Moreover, the standard deviation of pore sizes is proportional to their mean, suggesting that the larger the mean, the greater the fluctuation, and the smaller the mean, the less the fluctuation.

Furthermore, the individual pore's shape factor (F) is utilized to determine how regular the pore shape is, which is defined as

$$F = \frac{4\pi S_{\text{Pore}}}{P_{\text{pore}}} \tag{6}$$

where S_{pore} is the area of a closed individual pore in the random porous structures, and P_{pore} is the perimeter of this pore (Chua and Siow, 2016). The shape factor F is normally in the range of 0.0 to 1.0. The greatest shape factor F, evaluated at 1.0, is found in a circular pore. With increasing pore shape irregularity, the shape factor F steadily declines and endlessly converges to 0. The shape factor distributions for each sample group were statistically computed, with each sample's contribution to the distribution highlighted, as illustrated in Fig. 7. The figure not only shows the mean and standard deviation of the shape factors for each group, but also shows the shape factor distribution's first (Q1), second (Q2), and third quartiles (Q3). In Fig. 7 (*a*) to (*c*), the mean value

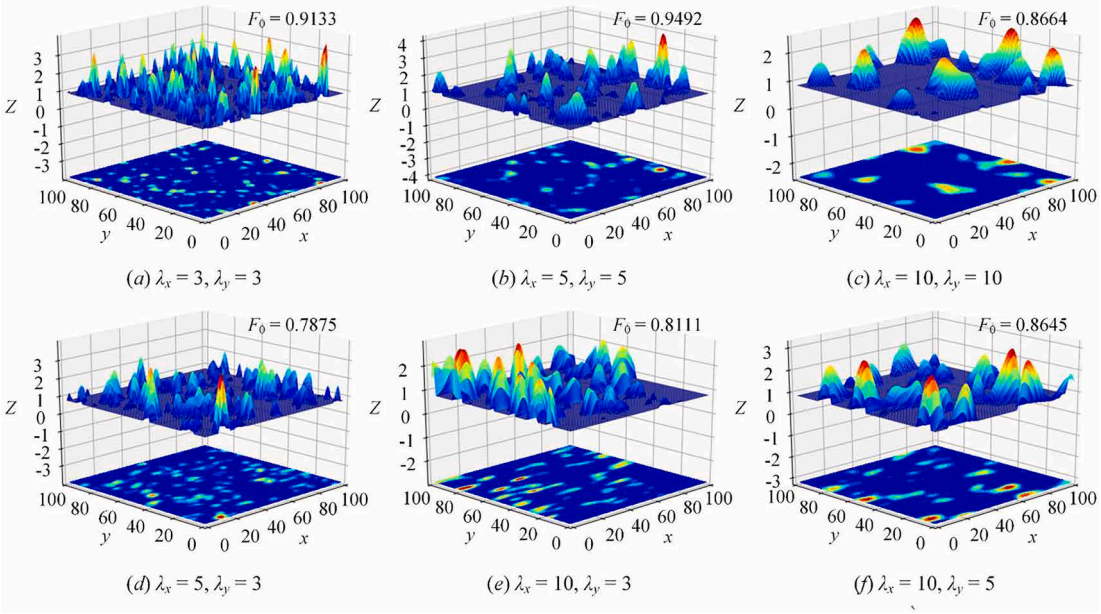

Fig. 3. One-cut Gaussian random field models with different combinations of λ_x and λ_y.

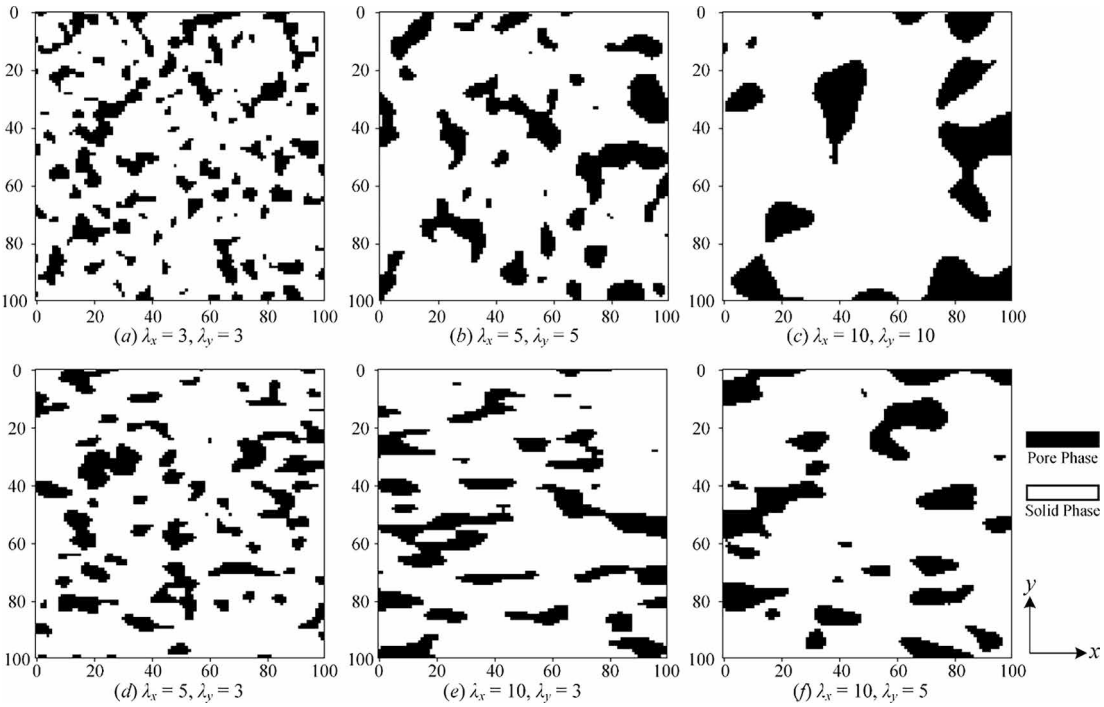

Fig. 4. Random porous structures with different combinations of λ_x and λ_y (Porosity = 20.0 %).

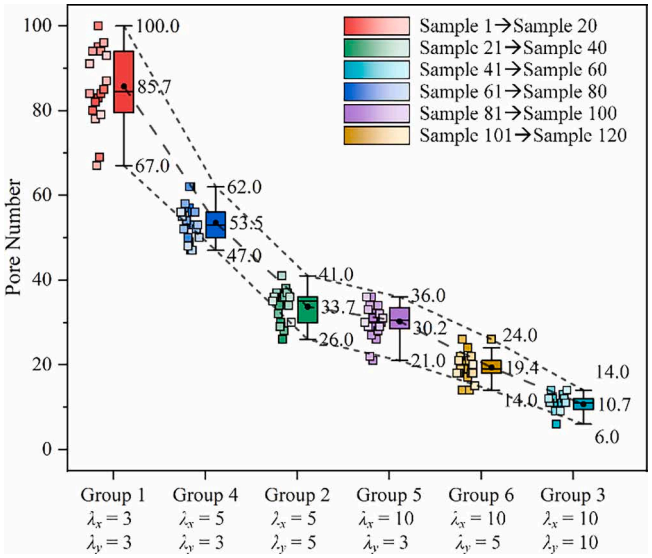

Fig. 5. The pore numbers in the random porous structures of the 120 random samples from the six groups with different combinations of λ_x and λ_y.

of the shape factors in the isotropic random samples drops as the correlation lengths grow, indicating that the pore shape becomes more irregular as the pore size increases. And once the correlation lengths expand, the standard deviation of the shape factor rises, implying that a larger pore size leads to greater pore shape fluctuations. Meanwhile, when the correlation length is increased, the values of Q1, Q2, and Q3 for the distributions decrease noticeably, that is, the shape factor distributions are skewed to the left, with a mean value decrease of 0.0445. According to Fig. 7 (*d*) to (*f*), the shape factor of the anisotropic random samples is positively connected with the ratio of λ_x and λ_y; in other words, the larger the ratio, the more irregular the pore shape. The standard deviations of the shape factor for anisotropic random porous samples follow a similar pattern to isotropic random samples, i.e., the larger the pore size, the greater the shape factor fluctuation. The values of Q1, Q2, and Q3 decline considerably as the ratio of the correlation length grows in the shape factor distributions, with the mean value of the shape factors reducing by 0.0877. In summary, the mean value of the shape factors is influenced dominantly by the correlation length ratio and the mean pore size, where the correlation length ratio is more influential. And the average pore size in the random porous samples has the most effect on the standard deviation of shape factors, namely, shape fluctuations. Based on the regularity and randomness of the pore distributions, a further study is conducted to investigate its effect on the mechanical properties and fracture behavior of random porous structures.

2.3. *Fracture phase-field model with high-accuracy degradation function*

The primary aim is to investigate the effects of pore sizes and shapes on the mesoscopic fracture processes and the macroscopic mechanical properties of the random porous structures. Here, the fracture phase-field model is selected to simulate the stress–strain responses of the silver nanoparticle solids. This phase-field method has the benefit of allowing numerical results to be derived from mesoscopic to macroscopic scales. In other words, this method can calculate the crack network formations for a given porous structure while also providing reasonable overall mechanical properties of the modeled material (Eid et al., 2021). Importantly, various types of degeneration functions have been used in previous studies for fracture phase-field models, such as quadratic-type (Miehe et al., 2010), cubic-type (Borden et al., 2012), quartic-type (Karma et al., 2001), single-parameter (Wilson et al., 2013), exponential-type (Sargado et al., 2018) degradation functions. For brittle fracture of random porous structures, particularly silver nanoparticles, a detailed and in-depth comparative analysis of the quadratic and exponential degradation functions is proffered in a one-dimensional

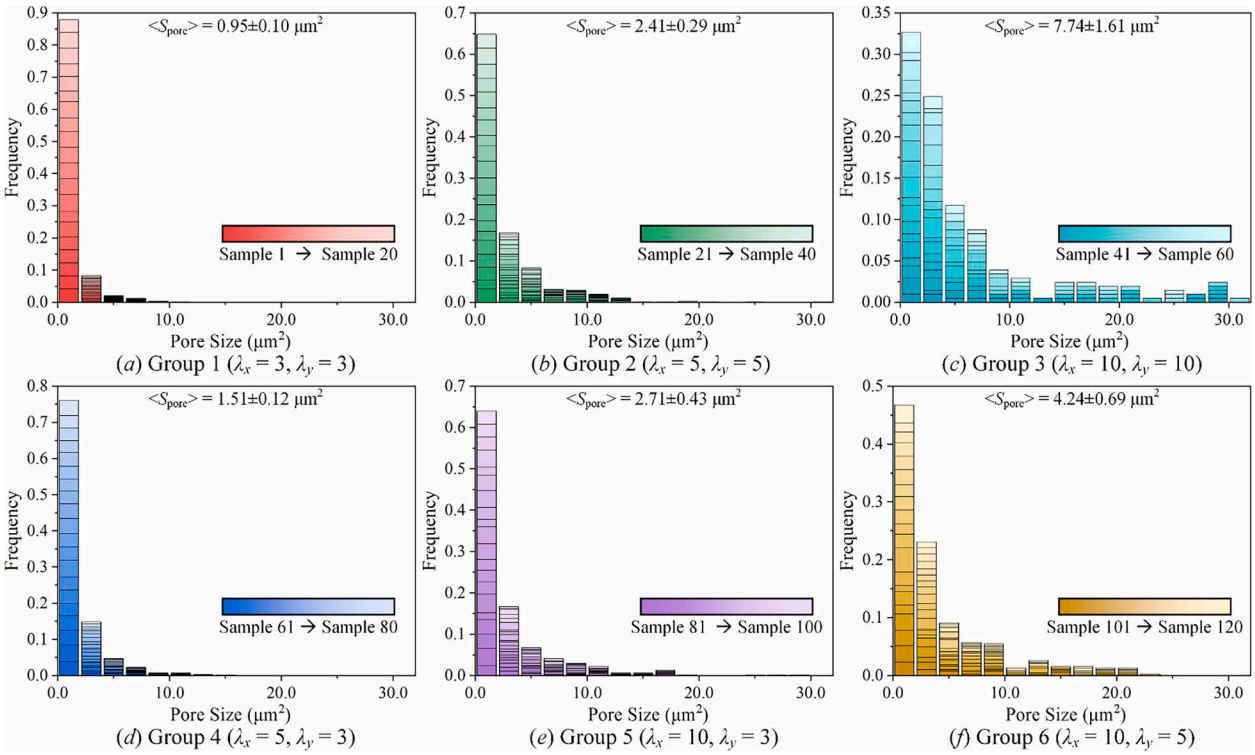

Fig. 6. The pore size distributions of the 120 samples from the six groups with different combinations of λ_x and λ_y.

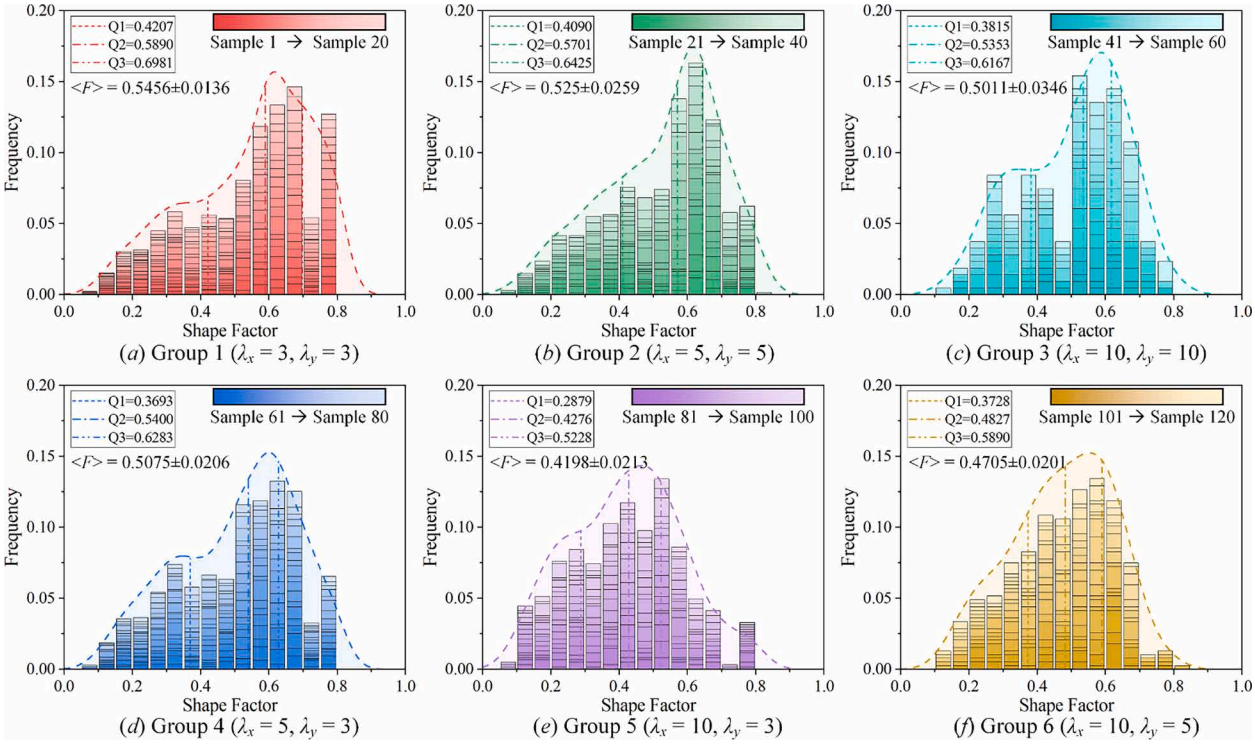

Fig. 7. The pore factor distributions of the 120 samples from the six groups with different combinations of λ_x and λ_y.

analytical model as shown in Appendix A. Based on the phase-field model with the preferred degradation function, the governing equations and numerical implementation are developed. The stress–strain responses of random porous structures during the fracture process are computed in the staggered iterative approach using Abaqus and its subroutines as computational foundations for the analysis of the pore distribution effects.

Based on the one-dimensional analytical model analysis, the fracture phase-field issues could be extended into the multi-dimensional case. Referring to the functionals of the total energy, the weak form of governing equations can be obtained as follow:

$$\int_{\Omega} g(\phi)\frac{d\psi}{d\epsilon} : \delta\epsilon \mathrm{d}\Omega - \int_{\Omega} \boldsymbol{b} \bullet \delta\boldsymbol{u}\mathrm{d}\Omega - \int_{\partial\Omega^t} \boldsymbol{t} \bullet \delta\boldsymbol{u}\mathrm{d}S = 0, \tag{7}$$

$$\int_{\Omega}\left[g^{'}(\phi)\psi(\epsilon)\delta\phi + \frac{g_c}{l}\left(\phi\delta\phi + l^2\nabla\phi \bullet \nabla\delta\phi\right)\right]\mathrm{d}\Omega = 0. \tag{8}$$

Meanwhile, the strong forms of the governing equations for the displacement are written as

$$\nabla\cdot[g(\phi)\sigma] + b = 0 on \Omega, \tag{9}$$

$$g(\phi)\sigma\cdot\boldsymbol{n} = \boldsymbol{t} on \partial\Omega^t, \tag{10}$$

$$\boldsymbol{u} = \overline{\boldsymbol{u}} on \partial\Omega^u. \tag{11}$$

and the strong forms for the phase-field value are given as

$$g_c l\nabla^2\phi - \frac{g_c}{l}\phi = g^{'}(\phi)\psi(\epsilon) \text{on} \quad \Omega, \tag{12}$$

$$\nabla\phi\cdot\boldsymbol{n} = 0 \text{on} \partial\Omega. \tag{13}$$

Because irreversible damage is assumed in this case, historical maximum strain energy is used to measure the amount of energy driving the fracture. In addition, as no damage occurs in the elastic phase, a phase-field threshold ϕ_c is proposed to differ between the damaged and intact status. The historical energy function $\mathscr{H}$ is defined as follows:

$$\mathscr{H}(t) = \begin{cases} \psi(\epsilon(t)) \text{if } \phi < \phi_c, \\ \max\limits_{s\in[0,t]}\psi(\epsilon(s)) \text{otherwise}, \end{cases} \tag{14}$$

where ϕ_c can be selected to match the experimental results referring to Fig. A. 2 and Fig. A. 3. Accordingly, equation (12) is updated as:

$$g_c l\nabla^2\phi - \frac{g_c}{l}\phi = -\frac{nk(1-\phi)^{n-1}e^{-k(1-\phi)^n}}{1-e^{-k}}\mathscr{H} \text{on} \quad \Omega. \tag{15}$$

The coupled system with displacement $\boldsymbol{u}$ and phase-field ϕ is given by

$$\boldsymbol{u} = \sum_{i=1}^{m}\boldsymbol{N}_i^{\boldsymbol{u}}\boldsymbol{u}_i \text{and} \phi = \sum_{i=1}^{m} N_i^{\phi}\phi_i, \tag{16}$$

where $\boldsymbol{N}_i^{\boldsymbol{u}}$ and $\boldsymbol{N}_i^{\phi}$ are the node i_{th} shape functions, and $\boldsymbol{u}_i$ and ϕ_i are the node i_{th} displacement and phase-field variables. Then, the derivatives of displacement and phase-field variable are expressed as

$$\epsilon = \sum_{i=1}^{\mathrm{M}}\boldsymbol{B}_i^{\boldsymbol{u}}\boldsymbol{u}_i \text{and} \nabla\phi = \sum_{i=1}^{M} B_i^{\phi}\phi_i, \tag{17}$$

where $\boldsymbol{B}_i^{\boldsymbol{u}}$ and B_i^{ϕ} are the derivative matrices of the shape functions. The residual vectors for displacement and phase-field are respectively considered as

$$\boldsymbol{r}_i^{\boldsymbol{u}} = \int_{\Omega} g(\phi)\left(\boldsymbol{B}_i^{\boldsymbol{u}}\right)^T\boldsymbol{\sigma}\mathrm{d}\Omega - \int_{\Omega}\left(\boldsymbol{N}_i^{\boldsymbol{u}}\right)^T\boldsymbol{b}\mathrm{d}\Omega - \int_{\partial\Omega_t}\left(\boldsymbol{N}_i^{\boldsymbol{u}}\right)^T\boldsymbol{t}\mathrm{d}S, \tag{18}$$

$$r_i^d = \int_{\Omega}\left\{g_c l\left(B_i^{\phi}\right)^T\nabla\phi - \left[\frac{nk(1-\phi)^{n-1}e^{-k(1-\phi)^n}}{1-e^{-k}}\mathscr{H} - \frac{g_c}{l}\phi\right]N_i^{\phi}\right\}\mathrm{d}\Omega. \tag{19}$$

Regarding a finite temporal increment $[t_m, t_{m+1}]$, the corresponding iteration with a Newton-Raphson nonlinear solver for numerical implementation can be written as

$$\begin{Bmatrix}\boldsymbol{u}\\ \phi\end{Bmatrix}_{m+1} = \begin{Bmatrix}\boldsymbol{u}\\ \phi\end{Bmatrix}_{k} - \begin{bmatrix}\boldsymbol{K}^{\boldsymbol{uu}} & 0\\ 0 & \boldsymbol{K}^{\phi\phi}\end{bmatrix}^{-1}\begin{Bmatrix}\boldsymbol{r}^{\boldsymbol{u}}\\ \boldsymbol{r}^{\phi}\end{Bmatrix}_{m}, \tag{20}$$

where

$$\boldsymbol{K}_{ij}^{\boldsymbol{uu}} = \frac{\partial\boldsymbol{r}_i^{\boldsymbol{u}}}{\partial\boldsymbol{u}_j} = \int_{\Omega} g(\phi)\left(\boldsymbol{B}_i^{\boldsymbol{u}}\right)^T\boldsymbol{C}_0\boldsymbol{B}_j^{\boldsymbol{u}}\mathrm{d}\Omega, \tag{21}$$

$$\begin{aligned}\boldsymbol{K}_{ij}^{\phi\phi} &= \frac{\partial r_i^{\phi}}{\partial\phi_j} \\ &= \int_{\Omega}\left\{g_c l\left(B_i^{\phi}\right)^T B_j^{\phi} - \left\{\frac{nk(1-\phi)^{n-2}e^{-k(1-\phi)^n}}{1-e^{-k}}\left[nk(1-\phi)^n - 1\right]\mathscr{H}\right.\right. \\ &\quad \left.\left. - \frac{g_c}{l}\right\}N_i^{\phi}\right\}\mathrm{d}\Omega,\end{aligned} \tag{22}$$

in which $\boldsymbol{C}_0$ is the material stiffness matrix.

Box 2
Staggered computational scheme for fracture phase-field modeling from t_m to t_m +1.

1. Initialization. Obtain historical energy $\mathscr{H}_m$, strain energy ψ_m, displacement $\boldsymbol{u}_m$, and phase-field ϕ_m at time t_m.
2. Update the historical energy. If the phase-field ϕ_m is less than ϕ_c, the updated historical energy $\mathscr{H}_{m+1}$ is ψ_m. Otherwise, the updated historical energy $\mathscr{H}_{m+1}$ is equal to the greater one of historical energy $\mathscr{H}_m$ and strain energy ψ_m.
3. Update the phase-field value. Utilizing the updated historical energy $\mathscr{H}_{m+1}$, the new phase-field ϕ_{m+1} is given by
$\phi_{m+1} = \mathrm{Arg}\left\{\inf\limits_{\phi}\int_{\Omega}\left[g(\phi)\mathscr{H}_{m+1} + g_c\gamma(\phi,\nabla\phi)\right]\mathrm{d}\Omega\right\}$.
4. Update the displacement. Based on the phase-field value ϕ_m, the updated displacement $\boldsymbol{u}_{\mathrm{m+1}}$ is computed by
$u_{m+1} = \mathrm{Arg}\left\{\inf\limits_{u}\int_{\Omega}[g(\phi)\psi(\epsilon) - \boldsymbol{b}\bullet\boldsymbol{u}]\mathrm{d}\Omega - \int_{\partial\Omega^t}\boldsymbol{t}\bullet\delta\boldsymbol{u}\mathrm{d}S\right\}$.
5. Update the strain energy. Using the obtained displacement $\boldsymbol{u}_{\mathrm{m+1}}$, the strain energy is calculated as
$\psi_{m+1} = g(\phi)\psi(\epsilon(\boldsymbol{u}))$.
6. Output the updated variables to next time increment t_{m+1}, including historical energy $\mathscr{H}_{m+1}$, strain energy ψ_{m+1}, displacement $\boldsymbol{u}_{m+1}$, and phase-field ϕ_{m+1}.

According to previous workflows (Arriaga and Waisman, 2018; Cao et al., 2020), a staggered computational scheme for fracture phase-field modeling is established as Box 2. Numerical simulations of random porous structures based on fracture phase-field modeling can be carried out using the proposed scheme. Material properties of sintered nanoparticle silver are listed in Table 1 regarding our previous works (Su et al., 2021). Notably, the length scale parameter l equals two times of the element size. For our porous structure, the radius of curvature ρ is at least half the element size, so that l is not much greater than ρ in our model.

3. Results

The numerical results of random samples, based on the Gaussian random field model and fracture phase-field model, are obtained by Abaqus and its subroutines. First, Gaussian random fields with a mean of 0 and a covariance of 1 are generated by python codes for 21 different combinations of λ_x and λ_y. The generated Gaussian random fields contain 6 groups of isotropic random spatial distributions and 15 groups of vertically flattened random spatial distributions. λ_x and λ_y are 3, 4, 5, 6, 8, and 10, respectively, for isotropic Gaussian random fields. Furthermore, λ_x is bigger than λ_y for vertically flattened Gaussian random fields. As a result, for a total of 15 groups, the combinations of λ_x and λ_y are chosen from the values 3, 4, 5, 6, 8, and 10. A total of 420 samples were collected, with 20 samples taken for each combination of λ_x and λ_y. This work focuses on the effect of pore size and shapes on random porous structures without the influence of porosity. Thus, the optimization algorithm in Box 1 produces 420 random porous structures with a fixed porosity of 0.2. Then, the random porous structures are imported into Abaqus CAE, and material properties and boundary conditions are constructed in the numerical models. The phase-field simulation of the random porous structure is realized by Abaqus and its subroutines, including USDFLD and UEL. Numerical experiments of the tensile test are carried out to analyze the mechanical properties and fracture behavior of the 420 samples with different combinations of λ_x and λ_y.

3.1. Results of the isotropic samples with the same λ_x and λ_y

The stress–strain response of the random porous structure can show mechanical behavior under tension, while the crack evolution and its effect on stress and strain in the structure can be studied using the fracture phase-field simulation. Three samples with the same λ_x and λ_y of 3, 5, and 10 are chosen and analyzed for isotropic random porous structures, as shown in Fig. 8. Upon reaching the maximum stress point, Fig. 8 (*a*)-(*c*) show cliff-like decreases in stress, with each decrease in stress corresponding to crack evolution in some structurally weak regions. Fig. 8 (*a*) indicates that random porous structures with small pores suffer small stress drops for each single crack formation, and the multiple and minor decreases result in an overall trend of gradual decrease. However, depicted in Fig. 8 (*c*), structures with large random pores appear to have a single rapid and sharp drop in stress, resulting in the rapid formation of a transverse crack. During the crack evolution process, the first crack in a random porous structure is located at the necking connection of two neighboring pores with large transverse sizes.

Table 1
Material properties of the sintered nanoparticle silver.

ρ	10 400 g/m^3
E	81.50 GPa
σ_{max}	300 MPa
ν	0.38
g_c	2.4 J/m^2
l	0.4 μm
n	3
k	2

As the cracks connect the pores, the updated porous network with the largest transverse size yields more cracks, forming larger networks until the computation is completed. Overall, as the feature lengths increase, the crack number decreases, and the average crack length increases for isotropic random porous structures. Remarkably, the longest transverse distance of the crack network has exceeded 70 percent of the structure length within a short time after the maximum stress point, and the subsequent structural strength finds difficulties in loading greater external stresses. Hence, the mechanical performances at the maximum stress point are highly crucial for the property degradation and fracture evolution of the random porous structure.

The von Mises stress distributions, maximum strain distributions, and historical energy distributions for different feature lengths are shown in Fig. 9 for structural performance under maximum stress. For the structure with small pores, stress and strain are distributed in more concentrated points in the porous network before approaching fracture, and this porous structure has more energy storage points, allowing more historical energy to be absorbed. Large pores, on the other hand, are subjected to concentrated stresses and strains at fewer points. A sudden fracture occurs at fewer points after maximum stress status, easily forming a penetration crack network and ultimately leading to structural failure.

3.2. Results of the vertically flattened samples with different λ_x and λ_y

The numerical results of vertically flattened random porous structures are achieved, for three samples shown in Fig. 10 with (*a*) $\lambda_x = 5.0$ and $\lambda_y = 3.0$, (*b*) $\lambda_x = 10.0$ and $\lambda_y = 3.0$, and (*c*) $\lambda_x = 10.0$ and $\lambda_y = 5.0$. Similarly, each stress–strain response has at least one rapid drop corresponding to the morphology of crack evolution. The average transverse length of the pores correlates with λ_x. The fracture occurs at the necking between two pores with a longer transverse length, resulting in the production of numerous cracks that eventually unite to form a long transverse crack. The crack number of the random pore structure decreases as the λ_x grows larger, while the average crack length increases. In comparison to λ_x, λ_y has a minor effect on the crack number and length. The fracture process for the porous structure with a small pore size is slow, consistent with the isotropic random porous structure, and it takes longer to reach the maximum stress, as illustrated in Fig. 10 (*a*). The maximum stress is attained quickly in the random porous structure with large pores, and the fracture develops into structural collapse in a considerably shorter time, as seen in Fig. 10 (*b*) and (*c*).

Larger portions of the random porous structures have considerable stress and strain distributions for smaller λ_x during maximum stress, as shown in Fig. 11. Moreover, random porous structures with smaller transverse pore lengths display bigger regions with pronounced historical energies in the region of historical energy distribution, implying greater regions for energy storage. As a result, fracture energy in structures with smaller pore sizes is shown to be higher.

As depicted in Fig. 12, the stress–strain response of a longitudinally flattened sample with $\lambda_x = 3.0$ and $\lambda_y = 5.0$ is obtained to investigate the anisotropic properties of the spatial morphologies. During the fracture process, the longitudinally flattened sample exhibits a greater tensile strength than the vertically flattened sample. In addition, the longitudinally flattened sample has longer crack lengths than the vertically flattened sample, requiring greater fracture energy to form a penetration crack and cause material failure. In order to investigate the weakness direction of the random porous structures as well as the actual pressure-sintered Ag process, this paper focuses on vertically flattened samples.

The results for these six random structures have never been more consistent or representative. Therefore, the mechanical properties of 420 random samples are statistically analyzed, including Young's modulus, UTS, and average historical energy at maximum stress. The effects of pore size and shape on the mechanical properties are investigated in the following section.

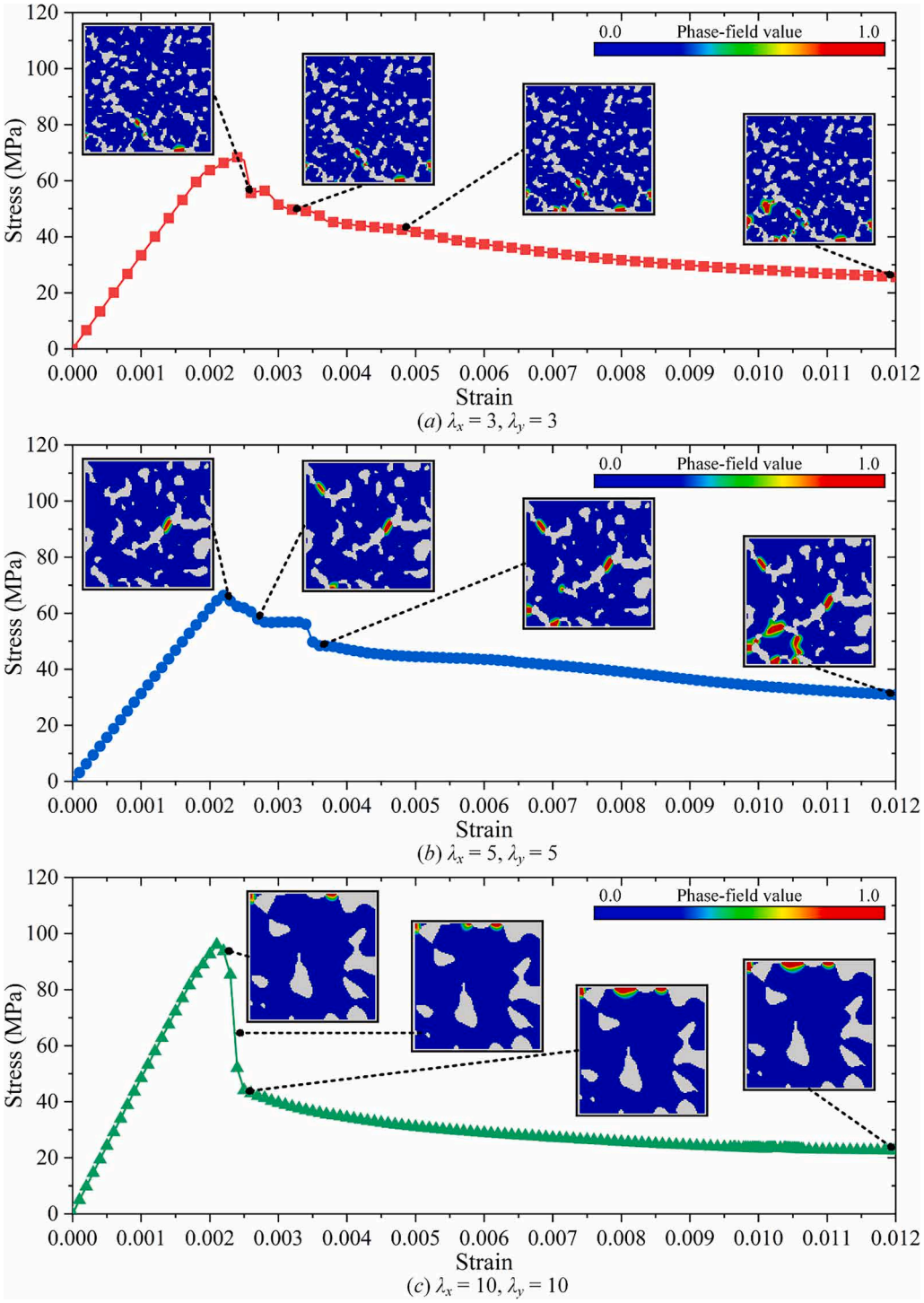

Fig. 8. Stress–strain responses with crack evolutions for isotropic random porous structures, where (*a*) $\lambda_x = 3.0$ and $\lambda_y = 3.0$, (*b*) $\lambda_x = 5.0$ and $\lambda_y = 5.0$, and (*c*) $\lambda_x = 10.0$ and $\lambda_y = 10.0$.

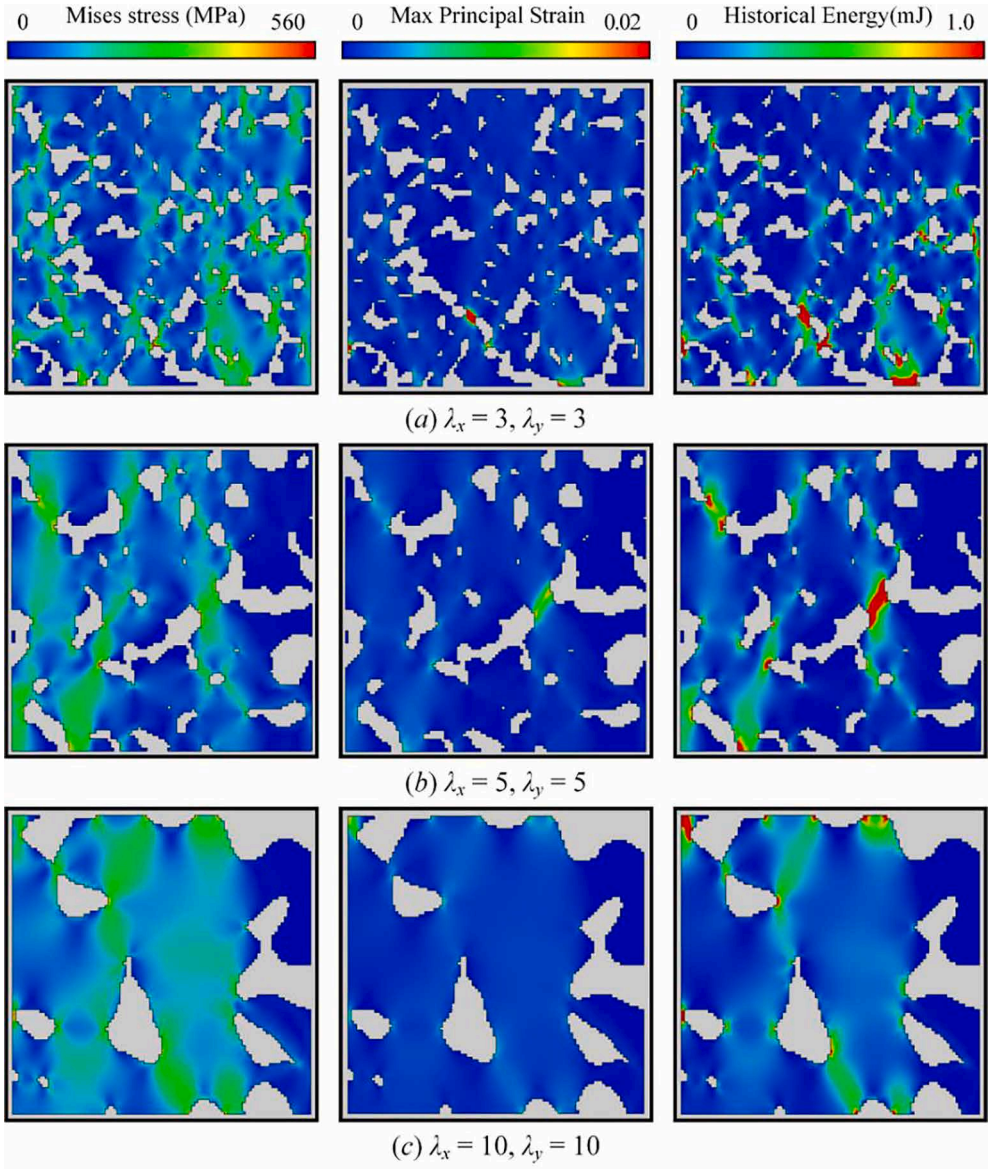

Fig. 9. The distributions of Mises stress, maximum principal strain, and historical energy for isotropic random porous structures, where (*a*) $\lambda_x = 3.0$ and $\lambda_y = 3.0$, (*b*) $\lambda_x = 5.0$ and $\lambda_y = 5.0$, and (*c*) $\lambda_x = 10.0$ and $\lambda_y = 10.0$.

4. Discussions

The random porous structure impacts the mechanical properties and fracture behavior, even with the same porosity. To begin, the material properties for 420 random samples are statistically investigated for random porous structures with various transversal and longitudinal feature lengths, including Young's modulus, UTS, and average historical energy at the maximum stress point. Furthermore, the effects of the mean, standard deviation, and maximum of pore sizes and shape factors on Young's modulus, UTS, and average historical energy at the maximum stress are analyzed for 420 random samples by Pearson correlation coefficients and corresponding P-values, to achieve a better understanding for random porous structures.

4.1. Young's modulus

Young's moduli of 420 random samples are individually calculated and statistically examined for various combinations of λ_x and λ_y, as shown in Fig. 13 and Fig. 14. Fig. 13 depicts Young's modulus of the random porous structure for each combination of λ_x and λ_y, where the dot color represents the ratio of λ_y to λ_x. Here, Young's modulus of random porous structures rises as λ_y/λ_x rises. In other words, the random porous structures with vertically flattened pores have a considerable negative impact on Young's modulus. Additionally, the fluctuation range of Young's modulus is influenced positively by λ_x, the transverse feature length of random porous structures. The large pores introduce significant uncertainties into Young's modulus, whereas the structure with small pores is considerably more stable in Young's modulus. Meanwhile, Young's modulus falls with decreasing λ_y for the same λ_x, implying that the longitudinal feature lengths of the random pores negatively affect the mean value of Young's modulus.

Fig. 14 illustrates the statistical distributions of Young's modulus grouped by λ_y/λ_x and λ_x for the calculated samples. As shown in Fig. 14 (*a*), the variance of Young's modulus distribution is nearly the same for different λ_y/λ_x, while the mean value is shifted to the right, indicating that the ratio improves Young's modulus. Fig. 14 (*b*) depicts the effect of λ_x on the statistical distribution of Young's modulus. The distribution curves shift to the left as the λ_x increases, changing from steep to flat. The larger the λ_x, the higher the variance and the lower the mean value of Young's modulus distribution.

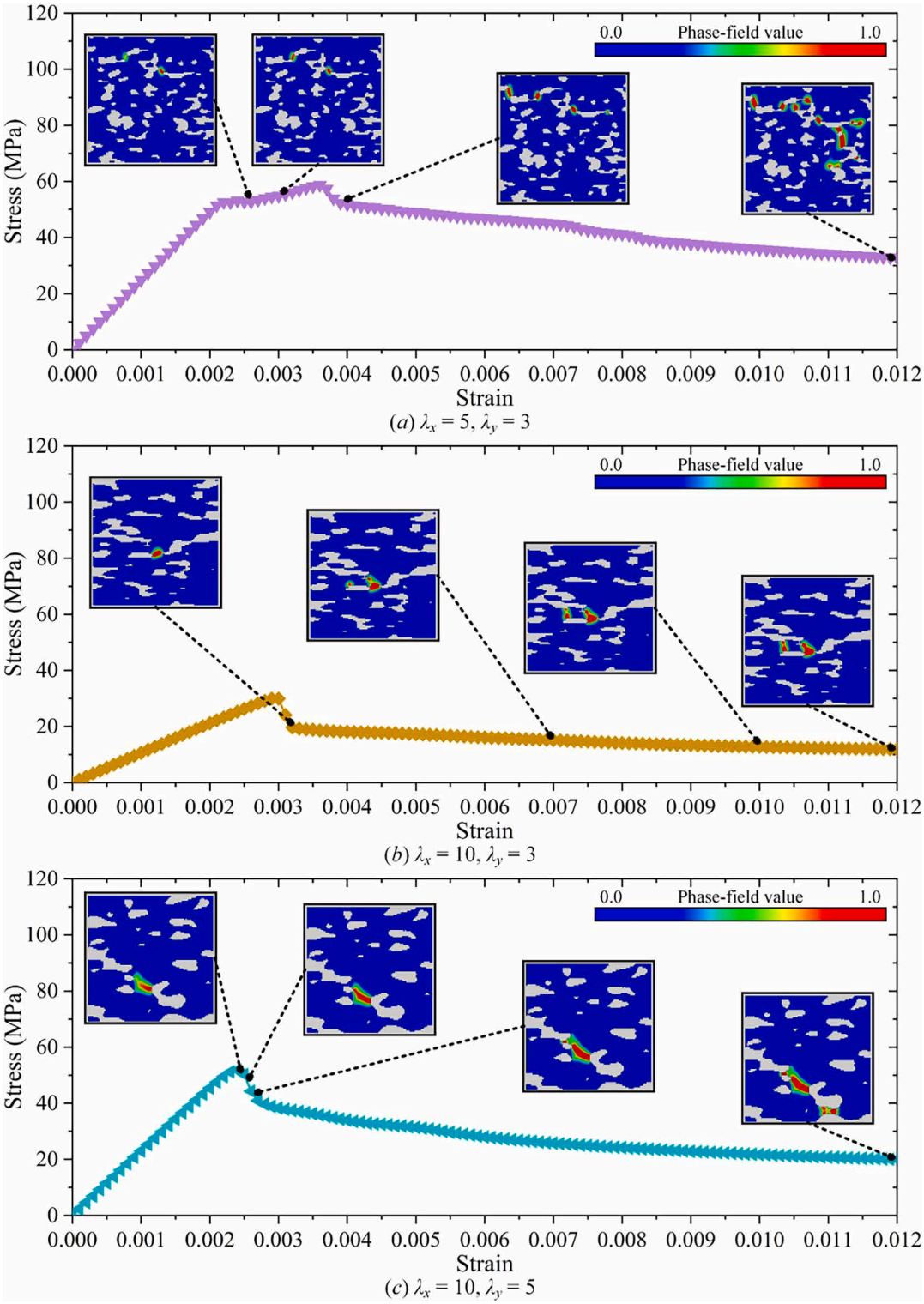

Fig. 10. Stress–strain responses with crack evolutions for vertically flattened random porous structures, where (*a*) $\lambda_x = 5.0$ and $\lambda_y = 3.0$, (*b*) $\lambda_x = 10.0$ and $\lambda_y = 3.0$, and (*c*) $\lambda_x = 10.0$ and $\lambda_y = 5.0$.

4.2. Ultimate tensile strength

Fig. 15 and Fig. 16 give the statistics and analysis of UTS for 420 random samples with various combinations of λ_x and λ_y. Fig. 15 illustrates the UTS of the random porous structure for each combination of λ_x and λ_y utilizing the λ_y/λ_x-dependent colored dots. The UTS of the random porous structures drops when the color goes from blue to red, and the λ_y/λ_x moves from large to small. λ_x influences the UTS data fluctuations, with larger λ_x resulting in larger fluctuations; and for the same λ_x, the larger the λ_y, the larger the UTS data mean and variance.

Fig. 16 provides the statistical distribution of the UTS data for various λ_y/λ_x and λ_x in more detail. The mean value of UTS in Fig. 16 (*a*) increases as the λ_y/λ_x increases, indicating that the isotropic random porous structure has a higher UTS than the flattened porous structure. Additionally, the variation of UTS grows with increasing λ_y/λ_x. For isotropic random porous structures, the UTS can be considered to be

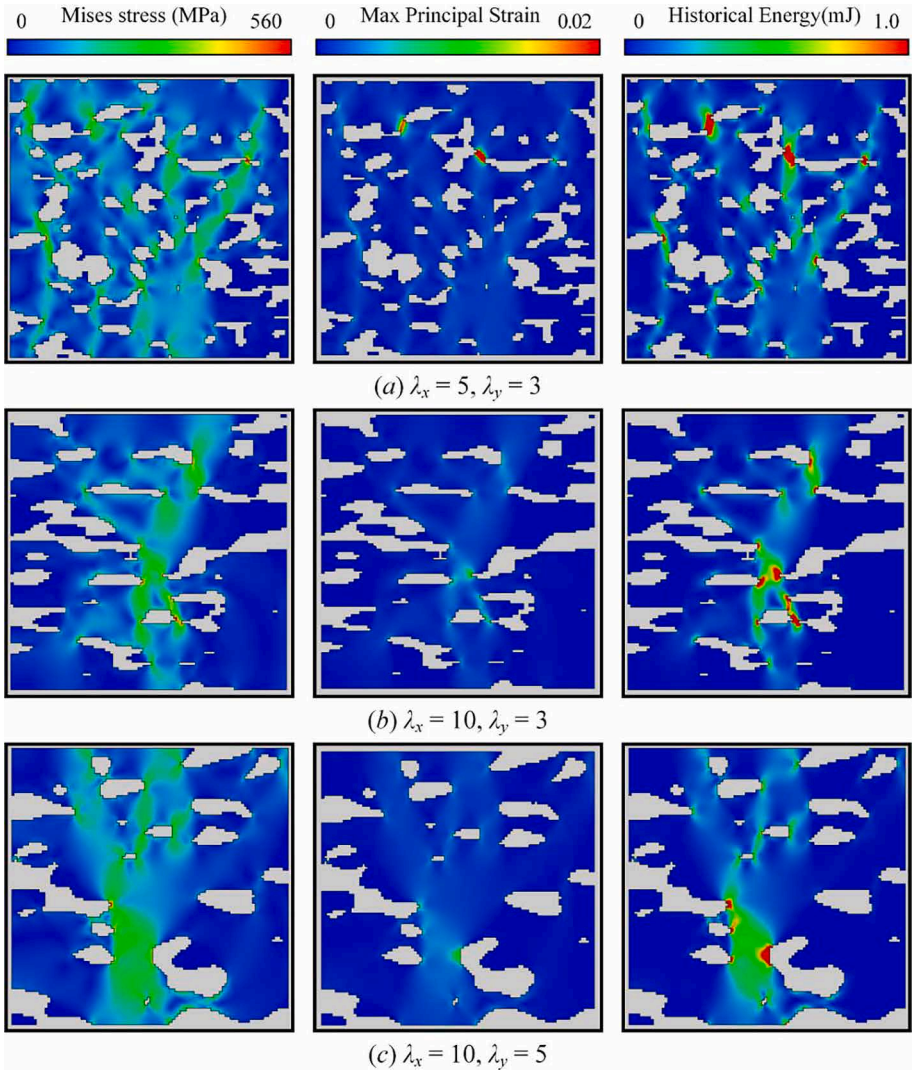

Fig. 11. Distributions of Mises stress, maximum principal strain, and historical energy for vertically flattened random porous structures, where (*a*) $\lambda_x = 5.0$ and $\lambda_y = 3.0$, (*b*) $\lambda_x = 10.0$ and $\lambda_y = 3.0$, and (*c*) $\lambda_x = 10.0$ and $\lambda_y = 5.0$.

more influenced by the randomness of pore distributions. As shown in Fig. 16(b), the UTS distribution curve evolves from a prominent peak on the left to a flattened one on the right when λ_x increases. The mean value and concentration of UTS are affected by λ_x values, with the bigger the λ_x, the smaller and more variable the UTS.

4.3. Average historical energy at the maximum stress point

Shortly after the maximum stress point, the crack usually propagates rapidly, with the percentage of the transverse size of the crack-connected pore network exceeding sixty percent, and a sharp fall in the stress weakens the structural ability to carry additional loads. Here, the average historical energies of the elements in random porous structures at the maximum stress point are calculated and analyzed. The average historical energy significantly represents the energy absorption of structural fracture and characterizes the global degradation of the structure due to historical energy-driven material degradation. Therefore, the average historical energies at the maximum stress point for 420 random samples are statistically analyzed in Figs. 17 and 18.

A scatter plot of the average historical energy of the 420 random samples, grouped by λ_x and λ_y, is shown in Fig. 17. The λ_y/λ_x has a significant impact on the average historical energy of the random porous structure, as indicated by the dot color. The historical energy at the maximum stress point is smaller with a smaller λ_y/λ_x, and the structure has poorer energy absorption performance. Meanwhile, as feature lengths increase, the average historical energy fluctuates widely and becomes more susceptible to the randomness of the structure.

Next, the average historical energy distributions grouped by λ_y/λ_x and λ_x are demonstrated in Fig. 18 (*a*) and (*b*). The mean and variance of the average historical energy distribution increase as λ_y/λ_x increases, and the distribution curve shifts from left to right, as shown in Fig. 18 (*a*). With the λ_x increasing, the mean of the average historical energy distribution falls, but the variance of the distribution rises, as shown in Fig. 18 (*b*).

4.4. Effect of pore size and shape factor

An approach of correlation analysis in statistics is used to describe and explain the relationships between the mechanical properties and the pore features of random porous structures to investigate the effect of pore size and shape factors. In this paper, the mechanical properties of random porous structures are discussed, including Young's modulus, UTS, and average historical energy at maximum stress point. And the pore features primarily focus on the pore size and shape factor's average value, standard deviation, and maximum value. The Pearson correlation coefficients with the P-values between the mechanical properties and the pore features for the 420 samples are computed, as shown in Fig. 19.

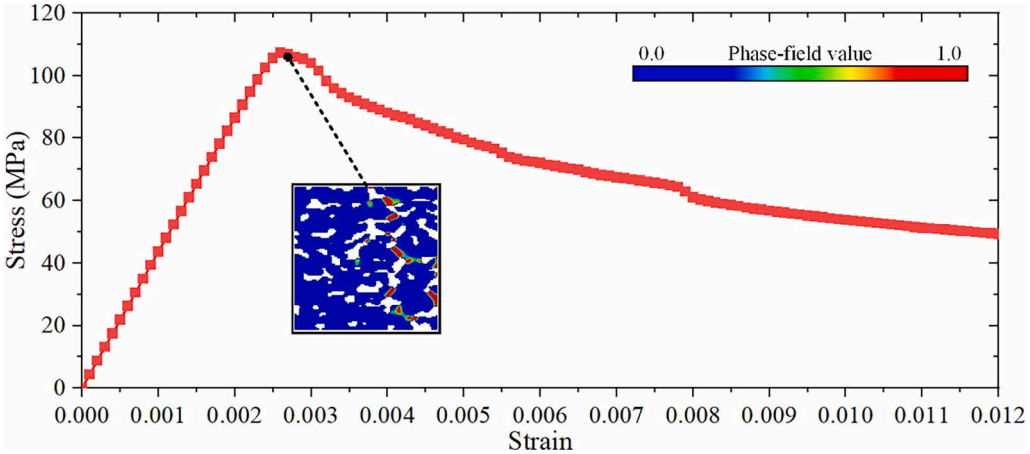

Fig. 12. Stress–strain responses with crack evolutions for longitudinally flattened random porous structures with $\lambda_x = 3.0$ and $\lambda_y = 5.0$.

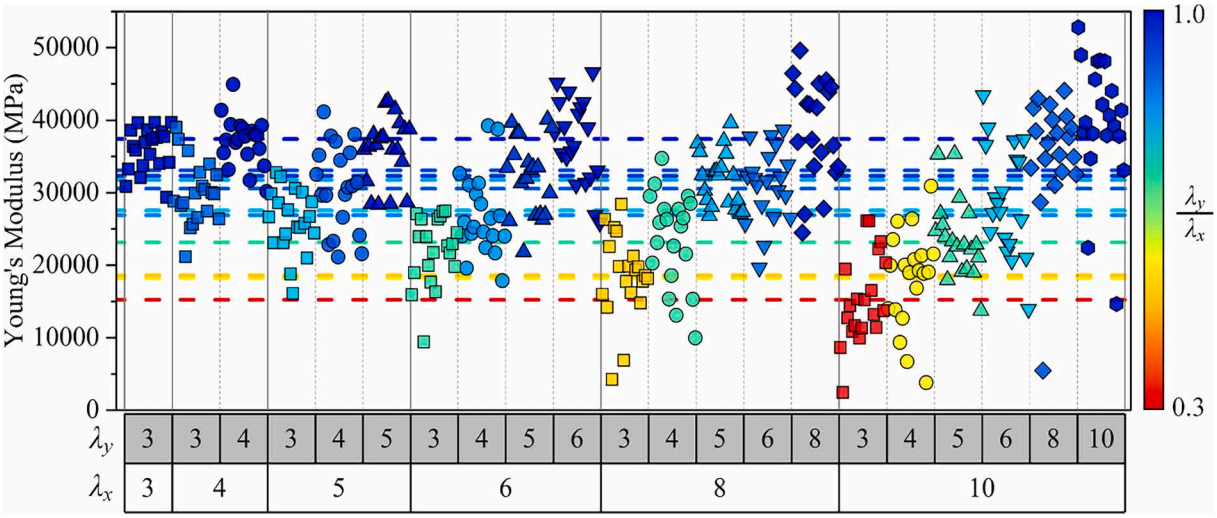

Fig. 13. The scatter plot of Young's modulus in various combinations of λ_x and λ_y for 420 random samples.

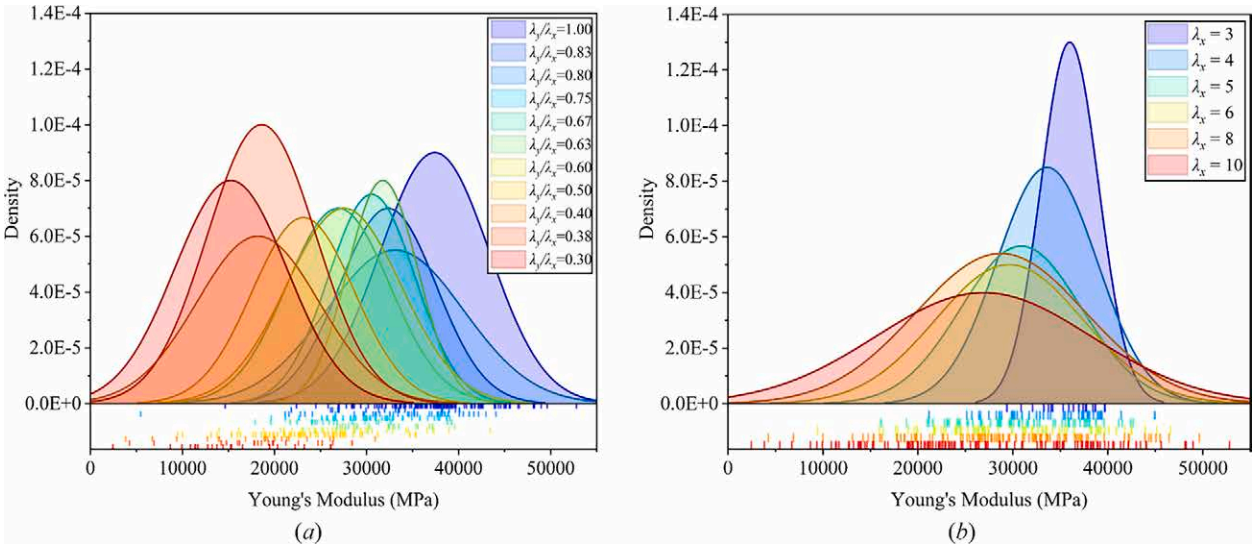

Fig. 14. Young's modulus distributions grouped by (*a*) λ_y/λ_x and (*b*) λ_x for 420 random samples.

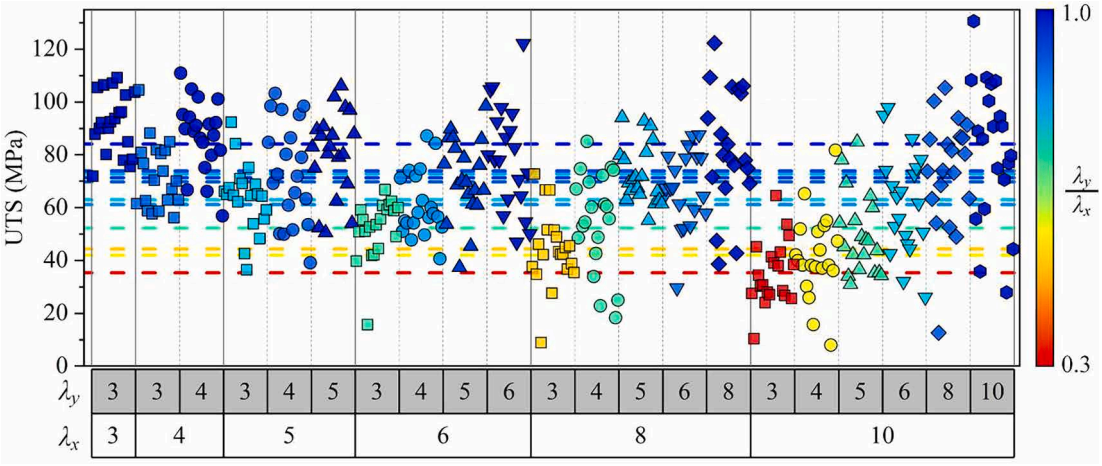

Fig. 15. The scatter plot of UTS in various combinations of λ_x and λ_y.

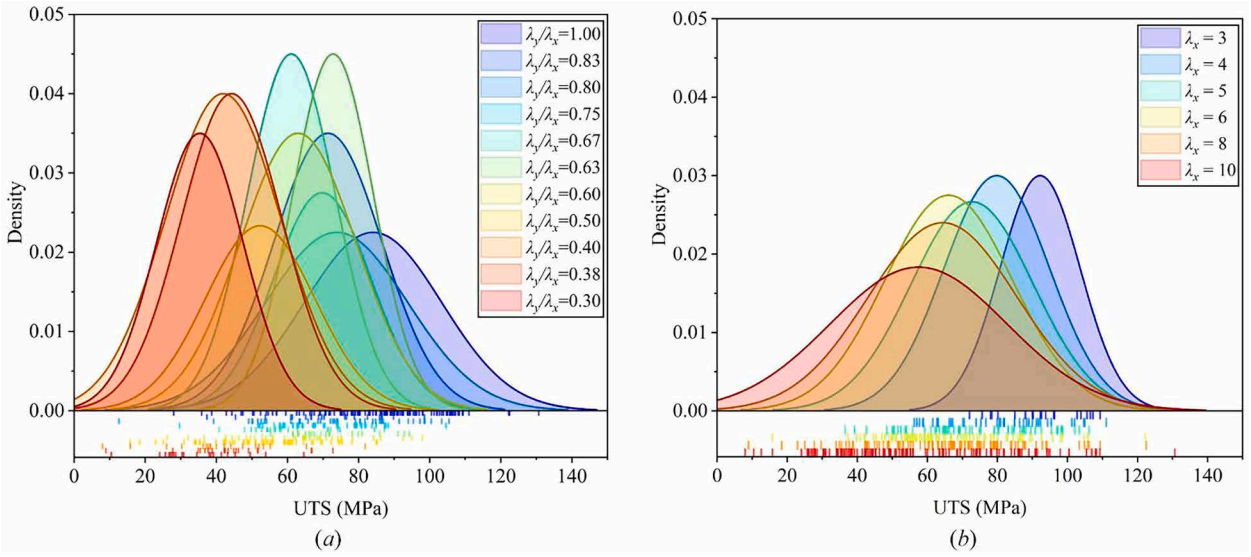

Fig. 16. UTS distributions grouped by (*a*) λ_y/λ_x and (*b*) λ_x for 420 random samples.

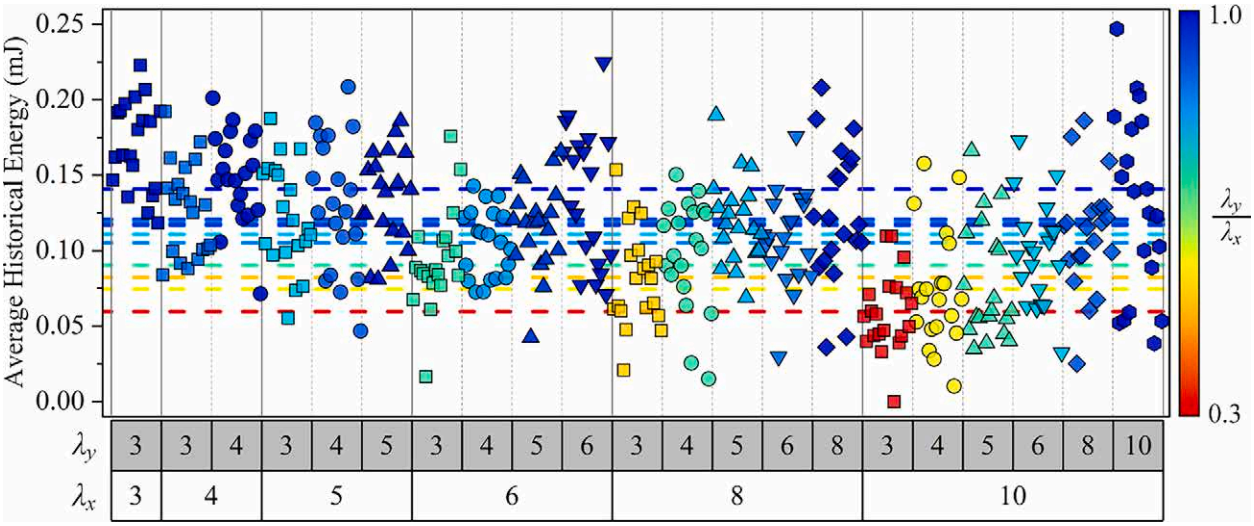

Fig. 17. The scatter plot of average historical energy at maximum stress point in various combinations of λ_x and λ_y.

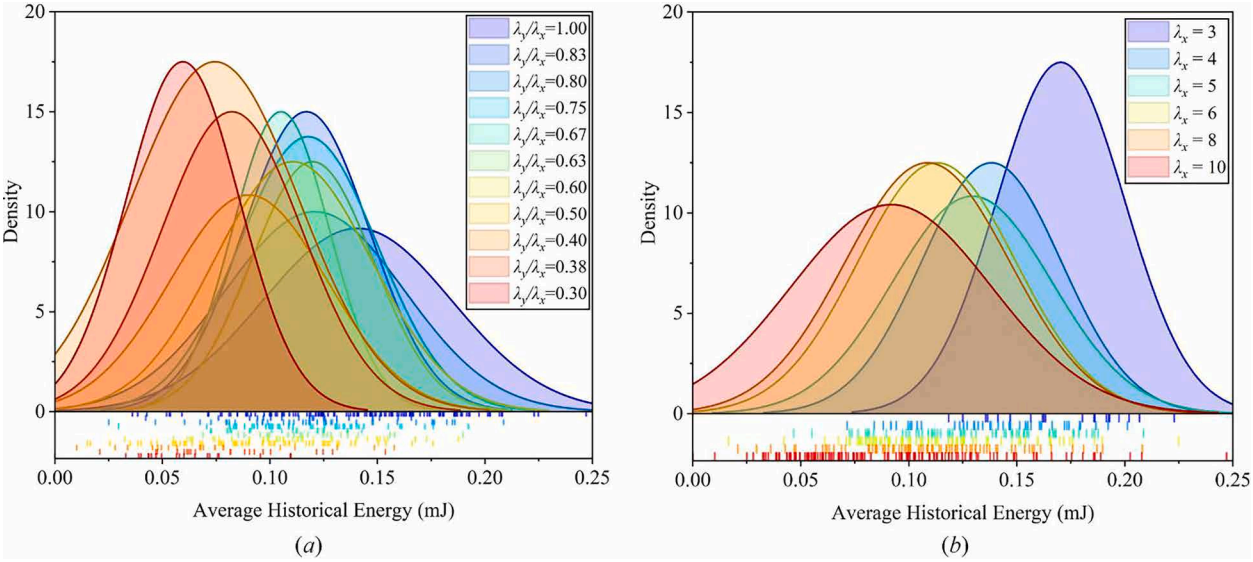

Fig. 18. Average historical energy distributions grouped by (*a*) λ_y/λ_x and (*b*) λ_x for 420 random samples.

The coefficients with the P-values allow us to evaluate not only the correlations between every-two different parameters but also identify the significance of these correlations.

The pore size is inversely proportional to the pore number for a given porosity, capturing the overall features of the random porous structure. The average of the pore sizes in 420 random samples can be used to analyze the pore numbers, under the same porosity and total area, for effect on the mechanical properties and fracture performances of the random porous structure.

The pore size average and standard deviation have a significant positive correlation with Young's modulus. However, the maximum value of pore sizes is irrelevant to Young's modulus. Young's modulus is primarily influenced by the overall features of pore size rather than the maximum pore size or weakest point, as evidenced by the insignificant effect of the maximum pore size. The smaller the average pore size, that is, the greater the pore number, the more uniformly the random porous structure can withstand stress distribution. At a small strain, the random porous structure with a small pore size distributes stresses uniformly in all corners, allowing for more stress concentration points. More points of stress concentration in fracture phase-field modeling imply phase-field rising and stiffness degradation of more elements in random porous structures, leading to a smaller Young's modulus. Furthermore, an increase in the average pore size will result in a larger standard deviation. Under the influence of the average pore size, the correlation between the

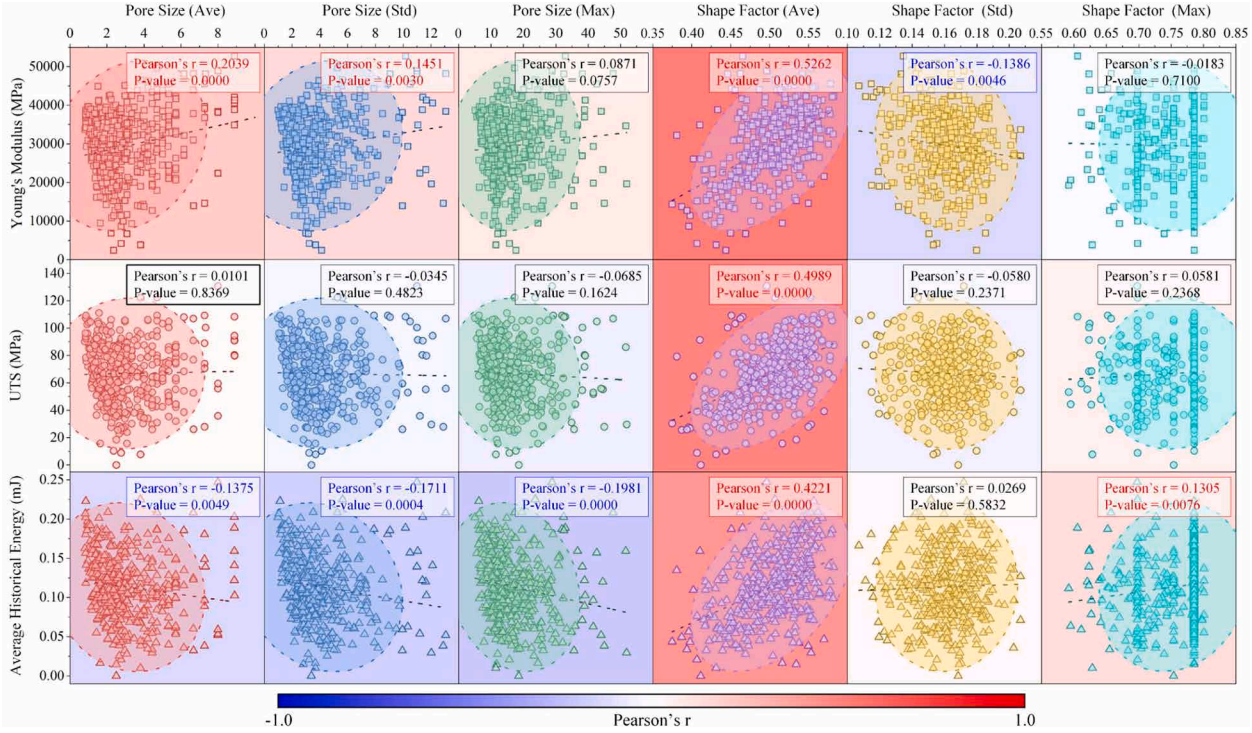

Fig. 19. Pearson correlation coefficients with the P-values between the mechanical properties and the pore features for the 420 samples, where the mechanical properties include Young's modulus, UTS, and average historical energy at a maximum stress point and the pore features contain the pore size and shape factor's average value, standard deviation, and maximum value.

standard deviation and Young's modulus is significant. The UTS is not significantly related to the pore sizes' average, standard deviation, and maximum values, as shown in Fig. 19. It is preferable that UTS is less sensitive to the global distribution of pore size and is more concerned with local features such as pore shape. The average, standard deviation, and maximum values of pore size are all significantly negatively correlated with average historical energy. The descending order of the Pearson correlation coefficients and the significance is the maximum, the standard deviation, and the average pore size. Here, the more energy the structure absorbs, the smaller the average pore size and the more uniform the pore distribution, implying a higher average historical energy. Moreover, the average historical energy at the maximum stress point could be the initial fracture point. With a larger maximum pore size, it is easier to crack at an earlier stage and suffer less historical energy. As a result, for random porous structures, a more uniform distribution of smaller pores increases the loading historical energy at the maximum stress point while decreasing Young's modulus. The shape factor is primarily concerned with the regularity of a single pore. The smaller the shape factor, the further a single pore deviates from circularity. Each pore's local features can be reflected by the shape factor. As shown on the right side of Fig. 19, the shape factors of each pore in each random porous structure are counted, and the average, standard deviation, and maximum values of the shape factors are given separately.

For 420 random samples, the average shape factor has a strong positive relationship with Young's modulus, UTS, and average historical energy at the maximum stress point, which has a more significant impact than pore size. Hence Young's modulus of the random porous structure increases when the pore shape is biased toward circularity. Because the strains around the circular pores are fairly uniformly distributed, more elements in the structure can participate in the stress loading. For the same small displacement, random porous structures with larger shape factors show larger reaction forces. Similarly, in the random porous structure with a larger shape factor, cracks are more difficult to formulate owing to the more uniform stress distribution, enabling a larger UTS of the structures. Meanwhile, due to the larger UTS, more historical energy is absorbed in the random porous structure at the maximum point. However, the standard deviation and maximum values of the shape factors are mostly unrelated to the mechanical properties, including Young's modulus, UTS, and average historical energy. Exceptionally, the standard deviation has a weakly negative relationship with Young's modulus, while the maximum value has a weakly positive relationship with the average historical energy. From a considerable perspective, Young's modulus tends to be influenced by the overall features, with the fluctuations in shape factor causing Young's modulus to decrease. In contrast, historical energy is more sensitive to local features, and the maximum value of the shape factor can affect energy absorption.

5. Conclusions and remarks

In this paper, a computational framework consisting of a Gaussian random field model and a fracture phase-field model is established to investigate the effect of pore feature distributions on the mechanical properties and fracture behavior of random porous structures. A one-cut Gaussian random field model is developed to efficiently generate the microstructure distributed with random pores with specific features in pore size, pore shape, and pore distribution. The pore size and shape factor of the random porous structure with fixed porosity are statistically analyzed, and the effect of different combinations of feature lengths on the pore size and shape factor is further investigated. The detailed analysis is performed based on our research in sintered silver nanoparticles, a typical random porous material. A fracture phase-field model with a high-accuracy degradation function for this material is created and discussed. Then, a reasonable strategy for determining the appropriate parameters of exponential degradation functions to match the actual mechanical response and fracture process is provided by the one-dimensional analytical fracture phase-field model.

Gaussian random fields have the advantage of being able to generate a large number of random samples. Accordingly, 21 combinations of feature lengths are chosen for random porous structures to generate 420 random samples with a porosity of 0.20. Using the numerical tensile results of 420 samples based on the phase-field model, we address the statistical properties of Young's modulus, UTS, and average historical energy at maximum stress point for different combinations of length features. Our findings show that the sum of feature lengths influences the variation of mechanical properties, whereas the feature length ratio shows the effects on the mean value of mechanical properties. Furthermore, Pearson correlation coefficients and their P-values are utilized to examine the relationships between mechanical properties such as Young's modulus, UTS, and average historical energy, and the statistics of pore size and shape components in random porous structures. One interesting finding is that the average pore size primarily represents the material's global properties and has a direct impact on Young's modulus. Another considerable outcome is that the maximum pore size shows some anisotropic local properties and influences negatively on the average historical energy. Moreover, the shape factor averages contribute to the stress distribution around every single pore and significantly affect Young's modulus, UTS, and average historical energy.

The numerical approach is primarily used to generate and analyze two-dimensional random porous structures. More studies can be done in the future to expand into the three-dimensional structure to gain a better understanding of the correlation of true microstructure with mechanical behavior. The relationship between three-dimensional spatial distribution features and mechanical properties can be investigated for random porous structures as well. On the basis of the *meso*-scale random porous structures, a macroscopic investigation, such as single-notched problems, can be conducted to gain additional insights. In addition, a huge number of random samples generated by our approach can be studied more effectively by machine learning. Efficient and fast links between random porous structure and mechanical characteristics can be developed by machine learning, which can drastically reduce computational consumption and achieve microstructure-based material attributes more quickly. In summary, the established method can be used to investigate the mechanical properties and fracture behavior of random porous structures subject to the variables related to their microstructural features. The certainty and uncertainty of random porous materials are being further explored by analyzing the statistical properties of pore features, which has the potential for reliability-based material design and optimization for numerous applications in the future.

Declaration of Competing Interest

The authors declare that they have no known competing financial interests or personal relationships that could have appeared to influence the work reported in this paper.

Data availability

Data will be made available on request.

Acknowledgments

This work was supported by the National Natural Science Foundation of China (No. 52175148), the Natural Science Foundation of Shaanxi Province (No. 2021KW-25), the Natural Science Foundation of Chongqing (No. CSTB2022NSCQ-MSX0574), and the National Key Laboratory Foundation 2022-JCJQ-LB-006 (No. 6142411232212). The authors also acknowledge the support from EPSRC (UK) research grants (No. EP/R004501/1 and No. EP/R032203/1).

Appendix A. One-dimensional analytical model analysis

To begin, the fracture phase-field model introduces a diffuse approximation of the sharp crack. An exponential crack phase-field function in a one-dimensional bar proposed by Miehe as

$$\phi(x) = \exp\left(-\frac{|x|}{l}\right), \tag{A.1}$$

where l is the length scale parameter. Its value is one at $x = 0$, and zero at $x \to \pm\infty$, shown in Fig. A1(a). Referring to Miehe (Miehe et al., 2010), a fracture surface of the phase-field function for the one-dimensional diffuse crack is introduced as

$$\Gamma = \int_\Omega \gamma(\phi, \phi')\mathrm{d}\Omega = \frac{1}{2l}\int_\Omega \left(\phi^2 + l^2\phi'^2\right)\mathrm{d}\Omega, \tag{A.2}$$

where $\gamma(\phi, \phi')$ is the crack surface density in one dimension. Integrating the work done by an external force, deformation, and fracture, the regularized total potential energy for the one-dimensional bar can be written as

$$\Pi = \Psi - W = \int_\Omega [g(\phi)\psi(\epsilon) + g_c\gamma(\phi, \phi')]\mathrm{d}\Omega - \int_\Omega b \bullet u\mathrm{d}\Omega - \int_{\partial\Omega^t} t \bullet u\mathrm{d}S, \tag{A.3}$$

in which $g(\phi)$ is the degradation function of phase-field value, $\psi(\epsilon)$ is the potential strain energy density, g_c is the energy release rate, Ω denotes the Dirichlet boundary condition of the body force b, and $\partial\Omega^t$ denotes the Neumann boundary condition of the traction t. Further, the variational equation of the total energy is obtained as

$$\delta\Pi = \int_\Omega g(\phi)\frac{\mathrm{d}\psi}{\mathrm{d}\epsilon} : \delta\epsilon\mathrm{d}\Omega - \int_\Omega b \bullet \delta u\mathrm{d}\Omega - \int_{\partial\Omega^t} t \bullet \delta u\mathrm{d}S + \int_\Omega \left[g'^{(\phi)}\psi(\epsilon)\delta\phi + \frac{g_c}{l}\left(\phi\delta\phi + l^2\phi'\delta\phi'\right)\right]\mathrm{d}\Omega. \tag{A.4}$$

This variational equation can be divided into two parts, comprising the weak form of the governing equations, one related to δu and the other related to $\delta\phi$, given by

$$\int_\Omega g(\phi)\frac{d\psi}{d\epsilon} : \delta\epsilon\mathrm{d}\Omega - \int_\Omega b \bullet \delta u\mathrm{d}\Omega - \int_{\partial\Omega^t} t \bullet \delta u\mathrm{d}S = 0, \tag{A.5}$$

$$\int_\Omega \left[g'(\phi)\psi(\epsilon)\delta\phi + \frac{g_c}{l}\left(\phi\delta\phi + l^2\phi'\delta\phi'\right)\right]\mathrm{d}\Omega = 0. \tag{A.6}$$

Accordingly, the equivalent strong form of the governing equations for the one-dimensional condition can be written as

$$\frac{d}{dx}\left(g(\phi)\frac{d\psi}{d\epsilon}\right) + b = 0 \mathrm{on}\Omega, \tag{A.7}$$

$$g(\phi)\psi'(\epsilon) = t \mathrm{on}\partial\Omega^t, \tag{A.8}$$

$$u = \overline{u} \mathrm{on}\partial\Omega^u, \tag{A.9}$$

$$g_c l\frac{d^2\phi}{dx^2} - \frac{g_c}{l}\phi = g'(\phi)\psi(\epsilon) \mathrm{on} \quad \Omega, \tag{A.10}$$

$$\frac{\mathrm{d}\phi}{dx} = 0 \mathrm{on}\,\partial\Omega. \tag{A.11}$$

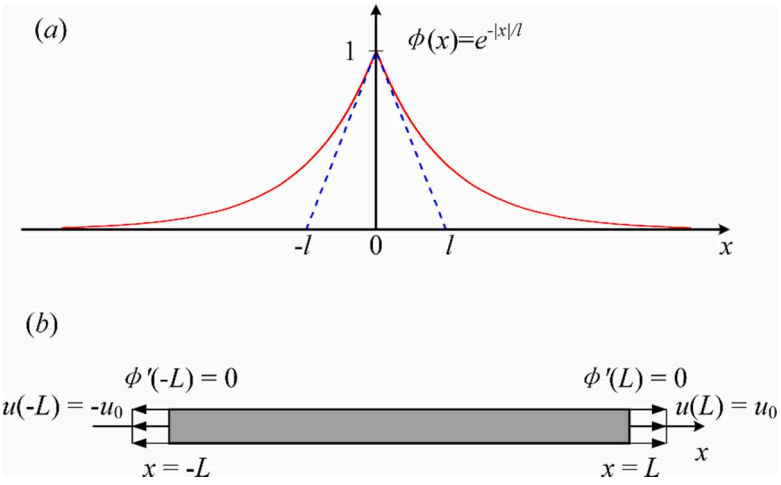

Fig. A1. (*a*) Phase-field for the diffuse crack with equation (A.1). (*b*) Boundary conditions for a 1D tensioned bar.

Referring to Sargado (Sargado et al., 2018), the boundary conditions are set as those illustrated in Fig. A1(*b*), where the one-dimensional homogenous bar is from -*L* to *L* with $u(\pm L) = \pm u_0$ and $\phi'(\pm L) = 0$. Regarding $d\psi/d\epsilon = \sigma$ and the body force $b = 0$, the strong formulations of the governing equations can be simplified to

$$\frac{d}{dx}[g(\phi)\sigma(\epsilon)] = 0, \tag{A.12}$$

$$g_c l\frac{d^2\phi}{dx^2} - \frac{g_c}{l}\phi = g'(\phi)\psi(\epsilon). \tag{A.13}$$

For this one-dimensional problem, we deem the stress and phase-field value uniformly distributed across the bar without spatial irrelevance, i.e., $\sigma(x) \equiv \sigma$ and $\phi(x) \equiv \phi$. Equations (A.12) and (A.13) are reduced to

$$-\frac{g_c}{l}\phi = g'(\phi)\psi(\epsilon). \tag{A.14}$$

The strain energy driving the fracture can be computed using the material parameter E and the strain ϵ, given by

$$\psi(\epsilon) = \frac{1}{2}\sigma(\epsilon)\epsilon = \frac{1}{2}E\epsilon^2. \tag{A.15}$$

Substitute (A.15) into (A.14), we obtain the strain function $\epsilon(\phi)$, depending on the phase-field ϕ, derived as

$$\epsilon(\phi) = \sqrt{-\frac{2g_c\phi}{El g'(\phi)}}, \tag{A.16}$$

which represents the strain degradation process based on the given degradation function. Additionally, the relationship between the stress σ and the strain ϵ is defined as

$$\sigma = E\epsilon \tag{A.17}$$

Furthermore, the degraded stress $g(\phi)\sigma(\phi)$, derived from equations (A.16) and (A.17), shows the apparent status of the overall stress in the one-dimensional bar subjected to tension, shown as

$$g(\phi)\sigma(\phi) = g(\phi)E\epsilon(\phi) = \sqrt{-\frac{2Eg_c\phi[g(\phi)]^2}{lg'(\phi)}}. \tag{A.18}$$

To eliminate the dependency of the apparent stress and strain on the material parameters E, l, and g_c, representative stress $g(\phi)\sigma(\phi)\sqrt{l/Eg_c}$ and strain $\epsilon(\phi)\sqrt{El/g_c}$ are constructed with only respect to the phase-field value and its degradation function, displayed as

$$\epsilon(\phi)\sqrt{El/g_c} = \sqrt{\frac{-2\phi}{g'(\phi)}}, \tag{A.19}$$

$$g(\phi)\sigma(\phi)\sqrt{l/Eg_c} = \sqrt{\frac{-2\phi[g(\phi)]^2}{g'(\phi)}}. \tag{A.20}$$

As illustrated in analytical equations (A.19) and (A.20), the phase-field value and its degradation function play an essential role in the stress–strain response during the cracking processes under the phase-field description. That is, the degradation function can govern the corresponding stress–strain behavior directly. Hence, we draw attention to degradation functions with various parameter values that might characterize mechanical behavior throughout the material degrading process.

The typical quadratic-type degradation function is utilized as a baseline for the suitable stiffening processes to avoid the high phase field value of the damaged material, with the degradation function $g_2(\phi)$ and its first-order derivative function $g_2'(\phi)$ provided by

$$g_2(\phi) = (1-\phi)^2, \tag{A.21}$$

$$g_2'(\phi) = 2(\phi - 1). \tag{A.22}$$

By substituting (A.21) and (A.22) into (A.19) and (A.20), the representative strain expression of ϕ is derived as

$$\epsilon(\phi)\sqrt{El/g_c} = \sqrt{\frac{\phi}{1-\phi}}, \tag{A.23}$$

and the representative strain expression of ϕ is given by

$$g(\phi)\sigma(\phi)\sqrt{l/Eg_c} = \sqrt{\phi(1-\phi)^3}. \tag{A.24}$$

According to the above expressions, the strain value of the quadratic degradation function grows as the phase-field increases. The stress value, on the other hand, initially rises and subsequently falls. Fig. A2 depicts this baseline with the black dashed line.

Due to its high accuracy and excellent flexibility to quantify the material degradation, an exponential-type degradation function $g_e(\phi)$ with two attributes k and n is defined as (Sargado et al., 2018)

$$g_e(\phi; k, n) = \frac{1 - e^{-k(1-\phi)^n}}{1 - e^{-k}}, \tag{A.25}$$

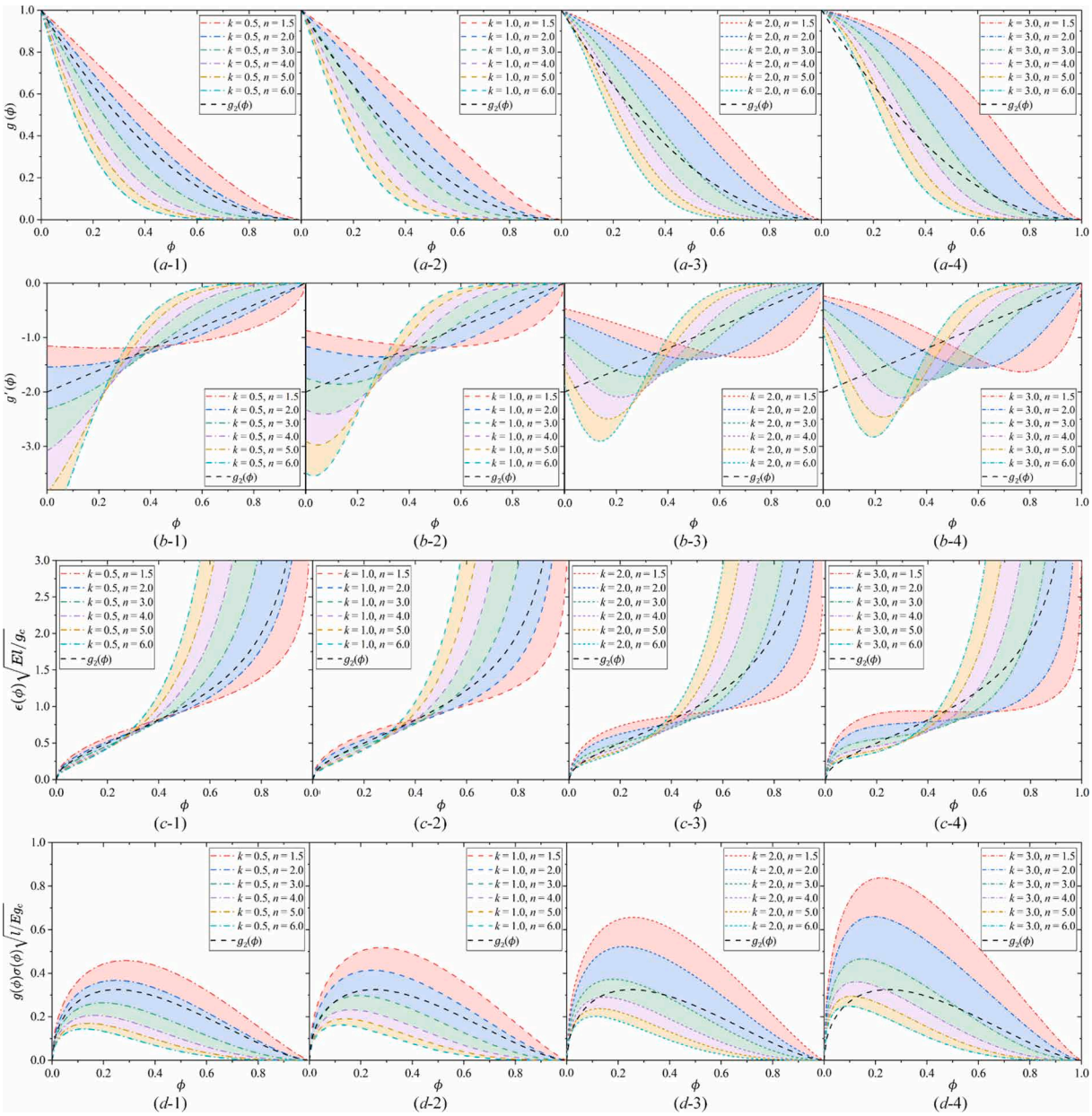

Fig. A2. Effect of different combinations of k and n on functions of the phase-field value. (a) the degradation function, (b) the derivative of the degradation function, (c) the representative strain function, and (d) the representative stress function.

and its first-order derivative function $g_e'(\phi)$ is expressed as

$$g_e^{'}(\phi;k,n) = -\frac{nk(1-\phi)^{n-1}e^{-k(1-\phi)^n}}{1-e^{-k}}. \tag{A.26}$$

Similarly, the analytical expressions of the apparent stress and strain are

$$\epsilon(\phi)\sqrt{El/g_c} = \sqrt{\frac{2\phi(1-e^{-k})}{nk(1-\phi)^{n-1}e^{-k(1-\phi)^n}}}, \tag{A.27}$$

and

$$g(\phi)\sigma(\phi)\sqrt{l/Eg_c} = \sqrt{\frac{2\phi[1-e^{-k(1-\phi)^n}]^2}{nk(1-\phi)^{n-1}(1-e^{-k})e^{-k(1-\phi)^n}}}. \tag{A.28}$$

Fig. A2 demonstrates the profiles of $g(\phi)$ and its derivative $g'(\phi)$, as well as the ϵ-ϕ and σ-ϕ curves for various combinations of k and n, where k ranges from 0.5 to 3.0 and n ranges from 1.5 to 6.0. Fig. A2 (a)-1, (a)-2, (a)-3, and (a)-4 show a continuous degradation of material stiffness with the increasing phase-field value. When the phase-field value is zero, the degradation function value is one, indicating that the material is undamaged. For a phase-field value of one, however, the material entirely failed with a degradation value of zero. As the baseline of the degradation function, $g_2(\phi)$ characterizes the

convex function, implying that as the phase-field value increases, the degradation rate of the material decreases. Fig. A2 (*a*)-1 shows that for $k = 0.5$, the degradation functions $g_e(\phi)$ are convex, which is consistent with $g_2(\phi)$. As k increases, the degradation function gradually shifts from an overall convex function to a profile with varying degradation rates associated with pre-increasing and post-decreasing. Besides the effect of k, a greater n causes an overall downward depression in the degradation function, increasing the degradation rate in the front section. Fig. A2 (*b*)-1, (*b*)-2, (*b*)-3, and (*b*)-4 show more detailed illustrations of the degradation rate variation trend, where the degradation rate is negative, in agreement with Fig. A2 (*a*).

Fig. A2 (*c*)-1, (*c*)-2, (*c*)-3, and (*c*)-4 depict the relationships between the representative strain and phase-field value, where the phase-field value runs from 0.0 to 1.0, and the strain varies from 0.0 to 3.0. The strain shows a positive correlation with the phase-field value. With phase-field values ranging from 0.0 to 0.4, k mostly impacts the increase rate of strain in the forward part of the curves for different degradation functions. Additionally, n influences the phase-field value at the last point ($\epsilon(\phi)\sqrt{El/g_c} = 3.0$) of the profile, that is the phase-field value of the broken material under the strain criteria. At the representative strain of 3.0, the phase-field value increases as n decreases. When n is large, the strain characteristics of brokenness appear even at low phase-field values. When n is 6.0, the phase-field value is nearly fractured around 0.6, which is inconsistent with the actual fracture situation. A smaller n gives a better indication of the actual fracture, particularly a brittle fracture.

Fig. A2 (*d*)-1, (*d*)-2, (*d*)-3, and (*d*)-4 depict typical stresses versus phase-field value. In this case, the phase-field value ranges from 0 to 1, and the stress rises from 0 to a maximum value before falling back to 0. k has a positive effect on the ascent rate in the stress-rising zone. However, n corresponds to the maximum stress with a negative correlation. To summarize, a larger k and a smaller n can better represent a delayed decline up to maximum stress and a fast degradation after maximum stress, also known as a brittle fracture.

Fig. A3 demonstrates the stress–strain responses in the one-dimensional bar using the above combinations of k and n. The curves are single-peaked, climbing from zero to maximum stress and then decreasing from there to zero. The initial part of the rising phase in the curve, an approximately linear increase, displays the elastic properties of the material. The length of the elastic part grows as k increases. In the meantime, while n decreases, the

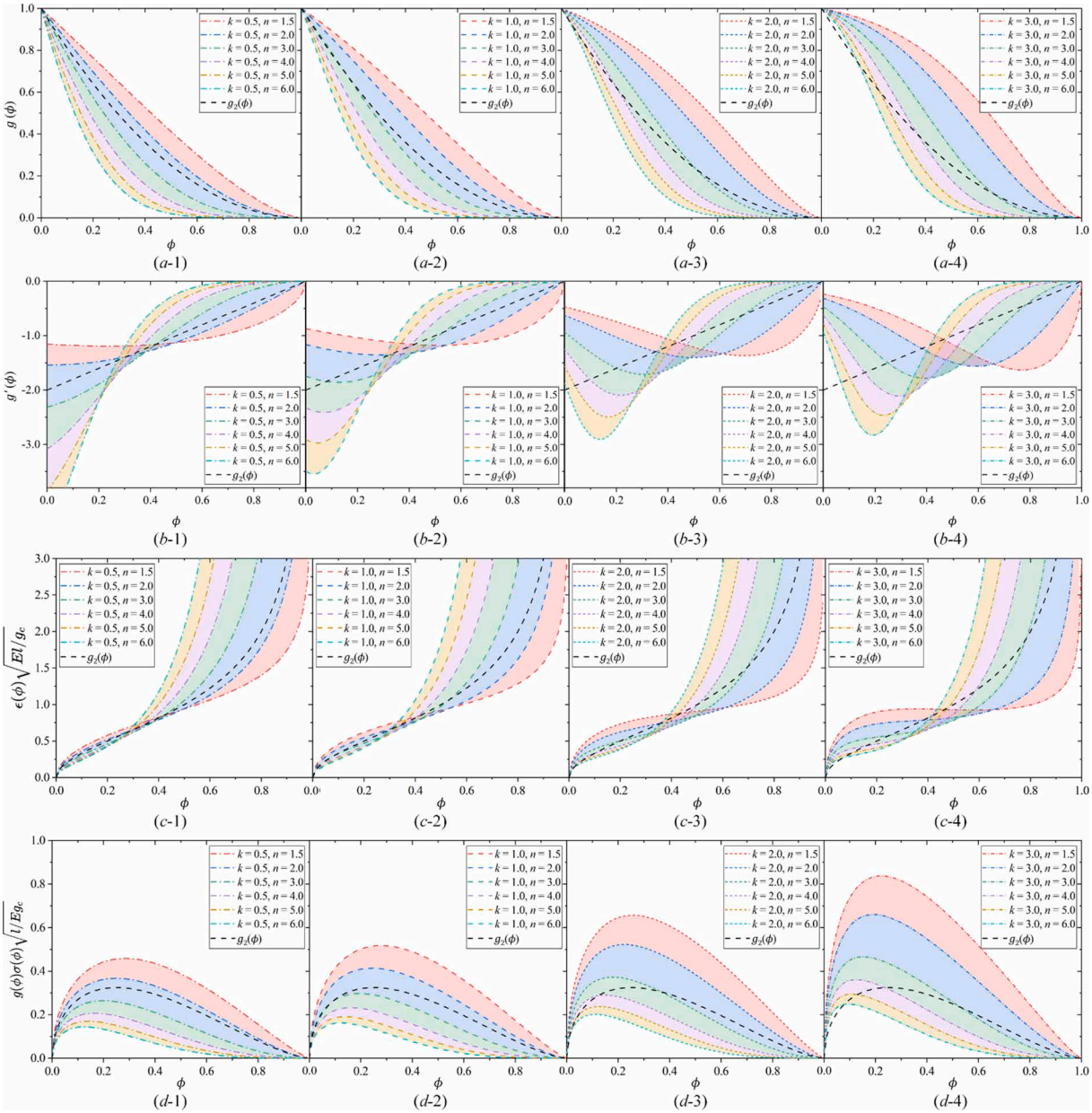

Fig. A3. The stress–strain response curves with the different combinations of k and n. (*a*) $k = 0.5$, (*b*) $k = 1.0$, (*c*) $k = 2.0$, and (*d*) $k = 3.0$.

length of the elastic part expands as well. Furthermore, the fracture rate is remarkable after the maximum stress point. The fracture rate of the baseline $g_2(\phi)$ is slow, and the material took an extended time to degrade to failure, which is incongruous with the actual fracture. As detailed in Fig. A3(*a*)-(*d*), a larger k combined with a smaller n allows the material to fracture quickly. As a result, the preferred k and n are selected to replicate the desired brittle fracture.

As shown in Fig. A3, the maximum stress point is a great representative, relating both mechanical properties and the fracture process. This point shows not only the tolerable stress ability of the material but also the phase-field degradation approaching the material fracture, which has a substantial impact on the fracture rate. Fig. A4 delves deeper into the maximum stress point. First, the baseline $g_2(\phi)$ is solved. Let the first-order derivative of the equation (A.24) be 0 to achieve the maxima, as follows:

$$\left[\sqrt{\phi(1-\phi)^3}\right]' = \frac{1}{2}\phi^{-\frac{1}{2}}(1-\phi)^{\frac{1}{2}}(1-4\phi) = 0, \tag{A.29}$$

Because ϕ ranges from 0.0 to 1.0, and the stress is zero when ϕ is 0.0 or 1.0. We obtain the maximum stress point at

$$\phi = \frac{1}{4}. \tag{A.30}$$

Further, the degradation value, strain, and stress are calculated as

$$g_2(\phi) = \frac{9}{16}, \tag{A.31}$$

$$\epsilon(\phi)\sqrt{El/g_c} = \frac{\sqrt{3}}{3}, \tag{A.32}$$

$$g(\phi)\sigma(\phi)\sqrt{l/Eg_c} = \frac{3\sqrt{3}}{16}. \tag{A.33}$$

When the brittle fracture occurs, the material has a rapid decline in stress and is broken shortly after passing the maximum stress point. However, the ϕ is 1/4 at the maximum stress point, and the $g_2(\phi)$ is only 0.5625, which is less than 0.60. With increasing ϕ, the degradation rate decreases unexpectedly, resulting in a delayed fracture. To select a reasonable k and n combination, the ϕ, $g_e(\phi)$, stress, and strain at the maximum stress point concerning n are given for various k, where n varies from 1.25 to 6.0 and k is 0.5,1.0,2.0, or 0.3, as shown in Fig. A4. The ϕ, $g_e(\phi)$, stress, and strain at maximum stress point all drop as n grows in Fig. A4 (*a*)-(*d*). Except for the decreasing trend of the ϕ, the $g_e(\phi)$, stress, and strain all increase significantly as k increases. In some suitable locations of Fig. A. 4, the combination of k and n is found and selected based on the actual maximum stress conditions. Here, k and n are determined with $g_e(\phi)$ greater than 0.75 the maximum stress point, and the stress and strain close to those of baseline g_2. In this case, k and n are chosen to be more than 2.0 and 2.0 to 3.5, respectively.

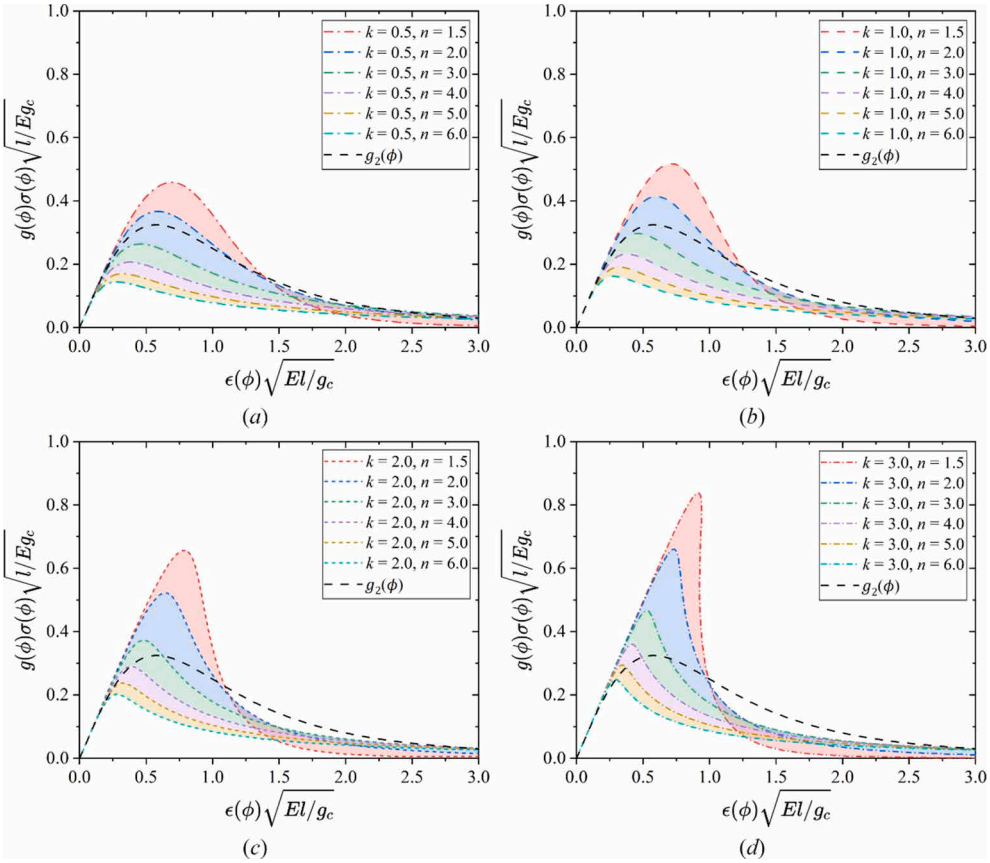

Fig. A4. Relationships between ϕ-related variables and n with various k at the maximum stress point. (*a*) ϕ, (*b*) $g(\phi)$, (*c*) stress, and (*d*) strain.

References

Arriaga, M., Waisman, H., 2018. Stability analysis of the phase-field method for fracture with a general degradation function and plasticity induced crack generation. Mech. Mater. 116, 33–48. https://doi.org/10.1016/j.mechmat.2017.04.003.

Blatny, L., Löwe, H., Wang, S., Gaume, J., 2021. Computational micromechanics of porous brittle solids. Comput. Geotech. 140, 104284 https://doi.org/10.1016/j.compgeo.2021.104284.

Borden, M.J., Verhoosel, C.V., Scott, M.A., Hughes, T.J.R., Landis, C.M., 2012. A phase-field description of dynamic brittle fracture. Comput. Methods Appl. Mech. Eng. 217–220, 77–95. https://doi.org/10.1016/j.cma.2012.01.008.

Burt, J.B., Helmer, M., Shinn, M., Anticevic, A., Murray, J.D., 2020. Generative modeling of brain maps with spatial autocorrelation. NeuroImage. 220, 117038 https://doi.org/10.1016/j.neuroimage.2020.117038.

Cao, Y.J., Shen, W.Q., Shao, J.F., Wang, W., 2020. A novel FFT-based phase field model for damage and cracking behavior of heterogeneous materials. Int. J. Plast. 133, 102786 https://doi.org/10.1016/j.ijplas.2020.102786.

Chen, C., Suganuma, K., 2019. Microstructure and mechanical properties of sintered Ag particles with flake and spherical shape from nano to micro size. Mater. Des. 162, 311–321. https://doi.org/10.1016/j.matdes.2018.11.062.

Chen, T., Yang, H., Bai, S., Zhang, Y., Guo, X., 2020. Facile preparation of high conductive silver electrodes by dip-coating followed by quick sintering. R. Soc. Open Sci. 7 (1), 191571.

Chen, H., Zhang, C., Lu, Q., Chen, H., Yang, Z., Wen, Y., Hu, S., Chen, L., 2019. A two-set order parameters phase-field modeling of crack deflection/penetration in a heterogeneous microstructure. Comput. Methods Appl. Mech. Eng. 347, 1085–1104. https://doi.org/10.1016/j.cma.2019.01.014.

Cheng, T.-L., Wen, Y.-H., Hawk, J.A., 2017. Modeling elasto-viscoplasticity in a consistent phase field framework. Int. J. Plast. 96, 242–263. https://doi.org/10.1016/j.ijplas.2017.05.006.

Chiappone, A., Gillono, M., Castellino, M., Bejtka, K., Rajan, K., Roppolo, I., Perrone, D., Bocchini, S., Ricciardi, C., Pirri, C.F., Chiolerio, A., 2018. In situ generation of silver nanoparticles in PVDF for the development of resistive switching devices. Appl. Surf. Sci. 455, 418–424. https://doi.org/10.1016/j.apsusc.2018.06.001.

Choe, C., Noh, S., Chen, C., Kim, D., Suganuma, K., 2018. Influence of thermal exposure upon mechanical/electrical properties and microstructure of sintered micro-porous silver. Microelectron. Reliab. 88–90, 695–700. https://doi.org/10.1016/j.microrel.2018.07.048.

Chua, S.T., Siow, K.S., 2016. Microstructural studies and bonding strength of pressureless sintered nano-silver joints on silver, direct bond copper (DBC) and copper substrates aged at 300 °C. J. Alloys Compd. 687, 486–498 https://doi.org/10/gjf2m7.

Ding, C., Liu, H., Ngo, K.D.T., Burgos, R., Lu, G.-Q., 2021. A Double-Side Cooled SiC MOSFET Power Module With Sintered-Silver Interposers: I-Design, Simulation, Fabrication, and Performance Characterization. IEEE Trans. Power Electron. 36, 11672–11680. https://doi.org/10.1109/TPEL.2021.3070326.

Duda, F.P., Ciarbonetti, A., Toro, S., Huespe, A.E., 2018. A phase-field model for solute-assisted brittle fracture in elastic-plastic solids. Int. J. Plast. 102, 16–40. https://doi.org/10.1016/j.ijplas.2017.11.004.

Eid, E., Seghir, R., Réthoré, J., 2021. Multiscale analysis of brittle failure in heterogeneous materials. J. Mech. Phys. Solids. 146, 104204 https://doi.org/10/ghh3jb.

Ernesti, F., Schneider, M., Böhlke, T., 2020. Fast implicit solvers for phase-field fracture problems on heterogeneous microstructures. Comput. Methods Appl. Mech. Eng. 363, 112793 https://doi.org/10.1016/j.cma.2019.112793.

Fang, J., Wu, C., Rabczuk, T., Wu, C., Ma, C., Sun, G., Li, Q., 2019. Phase field fracture in elasto-plastic solids: Abaqus implementation and case studies. Theor. Appl. Fract. Mech. 103, 102252 https://doi.org/10/ggz9v9.

Fuglstad, G.-A., Simpson, D., Lindgren, F., Rue, H., 2019. Constructing Priors that Penalize the Complexity of Gaussian Random Fields. J. Am. Stat. Assoc. 114, 445–452. https://doi.org/10.1080/01621459.2017.1415907.

Gao, Y., Jiao, Y., Liu, Y., 2021. Ultra-efficient reconstruction of 3D microstructure and distribution of properties of random heterogeneous materials containing multiple phases. Acta Mater. 204, 116526 https://doi.org/10/ghpn2p.

He, B., Schuler, L., Newell, P., 2020. A numerical-homogenization based phase-field fracture modeling of linear elastic heterogeneous porous media. Comput. Mater. Sci. 176, 109519 https://doi.org/10/gjgk5n.

He, B., Vo, T., Newell, P., 2022. Investigation of fracture in porous materials: a phase-field fracture study informed by ReaxFF. Eng. Comput. 1–17.

Jiang, Z., Chen, W., Burkhart, C., 2013. Efficient 3D porous microstructure reconstruction via Gaussian random field and hybrid optimization. J. Microsc. 252, 135–148. https://doi.org/10.1111/jmi.12077.

Jung, S., Chun, S.J., Shon, C.-H., 2016. Rapid Cellulose-Mediated Microwave Sintering for High-Conductivity Ag Patterns on Paper. ACS Appl. Mater. Interfaces. 8, 20301–20308. https://doi.org/10.1021/acsami.6b06535.

Karma, A., Kessler, D.A., Levine, H., 2001. Phase-Field Model of Mode III Dynamic Fracture. Phys. Rev. Lett. 87, 045501 https://doi.org/10.1103/PhysRevLett.87.045501.

Kuhn, C., Schlüter, A., Müller, R., 2015. On degradation functions in phase field fracture models. Comput. Mater. Sci. 108, 374–384. https://doi.org/10.1016/j.commatsci.2015.05.034.

Lee, Y.-J., Lee, J.-H., 2021. Effect of compression pressure on strength of low-temperature sinter bonding produced using silver formate. Powder Metall. 64, 235–240. https://doi.org/10.1080/00325899.2021.1916685.

Liu, Y., Li, J., Sun, S., Yu, B., 2019. Advances in Gaussian random field generation: a review. Comput. Geosci. 23, 1011–1047 https://doi.org/10/ghqkq6.

Liu, G.D., Wang, C., Swingler, J., 2021. Laser-Assisted Sintering of Silver Nanoparticle Paste for Bonding of Silicon to DBC for High-Temperature Electronics Packaging. Ieee Trans. Compon. Packag. Manuf. Technol. 11, 522–529. https://doi.org/10.1109/TCPMT.2020.3046917.

Marvi-Mashhadi, M., Vaz-Romero, A., Sket, F., Rodríguez-Martínez, J.A., 2021. Finite element analysis to determine the role of porosity in dynamic localization and fragmentation: Application to porous microstructures obtained from additively manufactured materials. Int. J. Plast. 143, 102999 https://doi.org/10.1016/j.ijplas.2021.102999.

Matsuhisa, N., Inoue, D., Zalar, P., Jin, H., Matsuba, Y., Itoh, A., Yokota, T., Hashizume, D., Someya, T., 2017. Printable elastic conductors by in situ formation of silver nanoparticles from silver flakes. Nat. Mater. 16, 834–840. https://doi.org/10.1038/nmat4904.

Miehe, C., Hofacker, M., Welschinger, F., 2010. A phase field model for rate-independent crack propagation: Robust algorithmic implementation based on operator splits. Comput. Methods Appl. Mech. Eng. 199, 2765–2778 https://doi.org/10/cj8qhp.

Miehe, C., Hofacker, M., Schänzel, L.M., Aldakheel, F., 2015. Phase field modeling of fracture in multi-physics problems. Part II. Coupled brittle-to-ductile failure criteria and crack propagation in thermo-elastic–plastic solids. Comput. Methods Appl. Mech. Eng. 294, 486–522 https://doi.org/10/f7rj5h.

Miehe, C., Dal, H., Schaenzel, L.-M., Raina, A., 2016. A phase-field model for chemo-mechanical induced fracture in lithium-ion battery electrode particles. Int. J. Numer. Methods Eng. 106, 683–711 https://doi.org/10/f8jtnm.

Mohd Zubir, N.S., Zhang, H., Zou, G., Bai, H., Deng, Z., Feng, B., Wu, A., Liu, L., Zhou, Y. N., 2019. Large-Area Die-Attachment Sintered by Organic-Free Ag Sintering Material at Low Temperature. J. Electron. Mater. 48 (11), 7562–7572.

Molnár, G., Gravouil, A., Seghir, R., Rethore, J., 2020. An open-source Abaqus implementation of the phase-field method to study the effect of plasticity on the instantaneous fracture toughness in dynamic crack propagation. Comput. Methods Appl. Mech. Eng. 365, 113004 https://doi.org/10/gg9v8p.

Neumann, M., Osenberg, M., Hilger, A., Franzen, D., Turek, T., Manke, I., Schmidt, V., 2019. On a pluri-Gaussian model for three-phase microstructures, with applications to 3D image data of gas-diffusion electrodes. Comput. Mater. Sci. 156, 325–331. https://doi.org/10.1016/j.commatsci.2018.09.033.

Okada, S., Nakahara, Y., Watanabe, M., Tamai, T., Kobayashi, Y., Yajima, S., 2019. Room-Temperature Sintering of Tri-n-Octylphosphine-Oxide-Capped Silver Nanoparticle Paste by Dipping into an Organic Solvent Containing a Sintering Agent. J. Phys. Chem. C. 123, 14118–14125. https://doi.org/10.1021/acs.jpcc.9b03378.

S. Chen, H. Zhang, Silver Sintering and Soldering: Bonding Process and Comparison, in: K.S. Siow (Ed.), -Attach Mater. High Temp. Appl. Microelectron. Packag. Mater. Process. Equip. Reliab., Springer International Publishing, Cham, 2019: pp. 1–33. https://doi.org/10.1007/978-3-319-99256-3_1.

Sanchez-Romaguera, V., Wünscher, S., Turki, B.M., Abbel, R., Barbosa, S., Tate, D.J., Oyeka, D., Batchelor, J.C., Parker, E.A., Schubert, U.S., Yeates, S.G., 2015. Inkjet printed paper based frequency selective surfaces and skin mounted RFID tags: the interrelation between silver nanoparticle ink, paper substrate and low temperature sintering technique. J. Mater. Chem. C. 3, 2132–2140. https://doi.org/10.1039/C4TC02693D.

Sargado, J.M., Keilegavlen, E., Berre, I., Nordbotten, J.M., 2018. High-accuracy phase-field models for brittle fracture based on a new family of degradation functions. J. Mech. Phys. Solids. 111, 458–489 https://doi.org/10/gc29zp.

Schuler, L., Ilgen, A.G., Newell, P., 2020. Chemo-mechanical phase-field modeling of dissolution-assisted fracture. Comput. Methods Appl. Mech. Eng. 362, 112838.

Stenzel, O., Pecho, O., Holzer, L., Neumann, M., Schmidt, V., 2017. Big data for microstructure-property relationships: A case study of predicting effective conductivities. AIChE J. 63, 4224–4232. https://doi.org/10.1002/aic.15757.

Su, Y., Fu, G., Liu, C., Liu, C., Long, X.u., 2021. Fatigue crack evolution and effect analysis of Ag sintering die-attachment in SiC power devices under power cycling based on phase-field simulation. Microelectron. Reliab. 126, 114244.

Su, Y., Fu, G., Liu, C., Zhang, K., Zhao, L., Liu, C., Liu, A., Song, J., 2021. Thermo-elasto-plastic phase-field modelling of mechanical behaviours of sintered nano-silver with randomly distributed micro-pores. Comput. Methods Appl. Mech. Eng. 378, 113729 https://doi.org/10/gh7zz6.

Tan, Y., Li, X., Chen, G., Gao, Q., Lu, G.-Q., Chen, X., 2020. Effects of thermal aging on long-term reliability and failure modes of nano-silver sintered lap-shear joint. Int. J. Adhes. Adhes. 97, 102488 https://doi.org/10.1016/j.ijadhadh.2019.102488.

Vazic, B., Abali, B.E., Yang, H., Newell, P., 2021. Mechanical analysis of heterogeneous materials with higher-order parameters. Eng. Comput. 1–17.

Watring, D.S., Benzing, J.T., Kafka, O.L., Liew, L.-A., Moser, N.H., Erickson, J., Hrabe, N., Spear, A.D., 2022. Evaluation of a modified void descriptor function to uniquely characterize pore networks and predict fracture-related properties in additively manufactured metals. Acta Mater. 223, 117464 https://doi.org/10.1016/j.actamat.2021.117464.

Wilson, Z.A., Borden, M.J., Landis, C.M., 2013. A phase-field model for fracture in piezoelectric ceramics. Int. J. Fract. 183, 135–153. https://doi.org/10.1007/s10704-013-9881-9.

Yin, B., Kaliske, M., 2020. Fracture simulation of viscoelastic polymers by the phase-field method. Comput. Mech. 65, 293–309. https://doi.org/10.1007/s00466-019-01769-1.

Zabihzadeh, S., Van Petegem, S., Holler, M., Diaz, A., Duarte, L.I., Van Swygenhoven, H., 2017. Deformation behavior of nanoporous polycrystalline silver. Part I, Acta Mater. 131, 467–474. https://doi.org/10.1016/j.actamat.2017.04.021.

Zein, S., Laurent, A., Dumas, D., 2019. Simulation of a Gaussian random field over a 3D surface for the uncertainty quantification in the composite structures. Comput. Mech. 63, 1083–1090 https://doi.org/10/ghqjn9.

Zerhouni, O., Brisard, S., Danas, K., 2021. Quantifying the effect of two-point correlations on the effective elasticity of specific classes of random porous materials with and without connectivity. Int. J. Eng. Sci. 166, 103520 https://doi.org/10.1016/j.ijengsci.2021.103520.

Zhang, L., Ji, H., Huang, H., Yi, N., Shi, X., Xie, S., Li, Y., Ye, Z., Feng, P., Lin, T., Liu, X., Leng, X., Li, M., Zhang, J., Ma, X., He, P., Zhao, W., Cheng, H., 2020. Wearable circuits sintered at room temperature directly on the skin surface for health monitoring. Acs Appl. Mater. Interfaces. 12, 45504–45515. https://doi.org/10.1021/acsami.0c11479.